UC Berkeley
UC Berkeley Electronic Theses and Dissertations

Title
Structural and Functional Studies of the K+/Cl- Cotransporter 4

Permalink
https://escholarship.org/uc/item/2544t7c0

Author
Reid, Michelle Soto

Publication Date
2023

Peer reviewed|Thesis/dissertation

eScholarship.org Powered by the California Digital Library
University of California

Structural and Functional Studies of the K^+/Cl^- Cotransporter 4

By

Michelle Soto Reid

A dissertation submitted in partial satisfaction of the

requirements for the degree of

Doctor of Philosophy

in

Molecular and Cell Biology

in the

Graduate division

of the

University of California, Berkeley

Committee in charge:

Professor Stephen Brohawn
Professor James Hurley
Professor Roberto Zoncu
Professor Sheng Luan

Spring 2023

Abstract

Structural and Functional Studies of the K^+/Cl^- Cotransporter 4

By

Michelle Soto Reid

Doctor of Philosophy in Molecular and Cell Biology

University of California, Berkeley

Assistant Professor Stephen Brohawn, Chair

Cation-chloride-cotransporters (CCCs) play critical roles in cellular volume regulation, neural development and function, audition, regulation of blood pressure, and renal function. Disruption of CCCs has been implicated in pathophysiology including epilepsy, hearing loss, and genetic disorders. In this study, we present the structure of a CCC, the *Mus musculus* K+-Cl- cotransporter (KCC) KCC4, determined by cryo-EM. The structure, captured in an inward-open conformation, reveals the architecture of KCCs and offers mechanistic insights into the function and regulation of this important transporter family. Our findings provide a structural explanation for the varied substrate specificity and ion transport ratio among CCCs, identify binding sites for substrate K+ and Cl- ions, and demonstrate the importance of key coordinating residues for transporter activity. These insights have significant implications for developing novel drugs and treatments targeting CCCs.

Table of Contents

List of figures and tables

List of Figures

List of tables

Acknowledgments

I am grateful to my dissertation advisor, Stephen Brohawn, for his guidance and support throughout my academic journey. His expertise, encouragement, and valuable insights have been instrumental in shaping my research and development as a scientist.

I extend my gratitude to my committee members, Jim Hurley, Roberto Zoncu, and Sheng Luan, for their time, attention, and constructive feedback. Their input helped to refine my work and further my understanding of the field.

I am deeply grateful to the faculty, staff, and trainees of the Molecular and Cell Biology Department for creating a welcoming and collaborative academic environment that supported my growth and success. I also want to extend special thanks to the individuals with whom I collaborated in running the Inclusive MCB program. Your hard work and dedication transformed our scientific community for the better and had a profound impact on my life. It was an honor to work with Lisa Eshun-Wilson, Kyle Tucker, Madeline Arnold, Amanda Gonzalez, Danielle Spitzer, Sonali Mali, Sophie Friesen, Diana Bautista, Iswar Hariharan, Carina Galicia, Hannah Bloom, Jim Hurley, Adam Yokom, David Kern, Christiane Vuofu, Michael Ly, and Kathleen Pestal. Thank you for your commitment to making our community more inclusive and supportive.

I would like to acknowledge my parents, John and Minerva, my siblings Jolen and Jenny, my husband Luis, my closest friend Minh, and my Tia Lupita and Tio Enrrique who have been my unwavering supporters throughout my academic journey.

Lastly, I would like to express my appreciation to the wonderful friends and colleagues I have met along the way, whose encouragement, advice, and companionship have been a constant source of inspiration and motivation.

Thank you all for your contributions and for being a part of my academic journey.

Chapter 1: Introduction to ion homeostasis and volume regulation

1.1 Overview

The activities within a cell are closely tied to the spatial organization of its internal macromolecular structures. Various physiological processes such as cell growth and division, changes in pH, exposure to hypo- or hypertonic media, and hormone signaling can lead to changes in cell volume which can result in significant disorganization and disruptions in vital cell activities. The cell's intrinsic regulatory mechanisms, such as regulatory volume decrease (RVD) and regulatory volume increase (RVI), activate specific metabolic and membrane-transport pathways to restore the initial cell volume. During abrupt volume changes, the transport of Na+, K+, Cl-, and organic osmolytes across the membrane is influenced by ion channels and transporters that affect the flow of water across the plasma membrane. The cation chloride cotransporters (CCCs) are of particular interest as they respond to changes in cell volume by modulating intracellular chloride concentration and transepithelial ion transport. Na+-dependent CCCs are activated during cell shrinkage or a decrease in $[Cl^-]_i$, while K+-dependent CCC members are inhibited. In contrast, during cell swelling or an increase in $[Cl^-]_i$, K+-dependent CCCs are activated while Na+-dependent members are inhibited. This chapter will cover the basics of membrane transporters, volume regulation, the cation chloride cotransporter family, and the regulatory mechanisms that control their activity during cell volume regulation.

1.2 Basics of membrane transporters

The field of membrane transporter biology has been steadily growing over the past decade and is now recognized for its significant role in our understanding of disease and treatments [26]. Membrane transporters can greatly impact drug pharmacokinetics, safety, and efficacy profiles [29], and their dysfunction is associated with various diseases, including obesity and cancers[26]. Therefore, understanding transport mechanisms and function is crucial for developing novel drugs and treatments.

Transporters facilitate the movement of small molecules, such as sugars, amino acids, nucleotides, inorganic ions, and drugs across the membrane. There are two types of transport, passive and active. Passive transport occurs through simple or facilitated diffusion, where molecules move down their electrochemical gradient without the use of protein carriers or energy input. Active transport, on the other hand, utilizes diverse energy-coupling mechanisms to move specific substrates against their concentration gradients. Active transporters are further subdivided (primary or secondary transport) depending on whether they directly convert photons or undergo chemical reactions like ATP hydrolysis to generate energy or use energy stored in ion gradients to drive the uphill transport of substrates, respectively.

Transporters are classified into three categories based on the orientation of substrate transport. Uniporters facilitate the transport of one substrate, while symporters/cotransporters transport at

least two substrates in the same direction. Antiporters transport two or more substrates in opposite directions. The cation chloride cotransporter family (CCCs) are secondary-active transporters that utilize the ion gradients of Na+ or K+ to move Cl- into or out of the cell to reach ion homeostasis and support cell volume regulation.

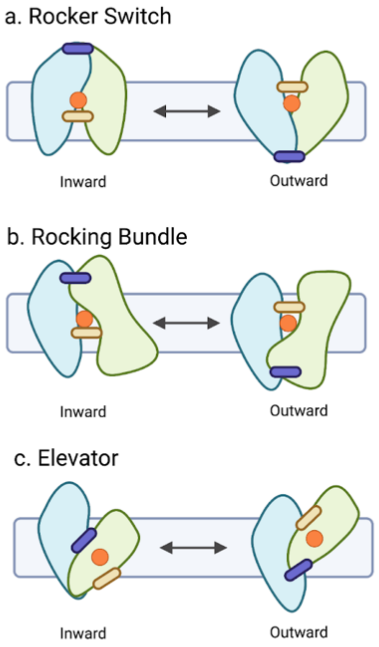

Figure 1: Alternating Access Mechanisms. Blue and green colors denote the transporter domains in the a) Rocker switch, b) Rocking bundle, and c) Elevator model. Figure adapted from Drew D, Boudker O. 2016.

Transporters have alternating intra- and extracellular gates that control access to the binding site, requiring global structural rearrangements for a full translocation cycle. Coupling of the gates occurs via alternating-access mechanisms: rocker-switch (Fig. 1A), rocking bundle (Fig. 1B), or elevator mechanism (Fig. 1C). In the rocker-switch mechanism, the two similar domains rock and expose the binding site to each side, while in the rocking bundle mechanism, two dissimilar domains rock against each other. The elevator mechanism involves a mobile domain that binds the ligand and traverses the membrane vertically against a rigid domain for translocation [15, 31].

Most transporters operate by the rocker-switch or rocking-bundle mechanism, with their structural fold correlating with the type of transport mechanism [37]. This mechanism is primarily observed in the major facilitator family (MFS) [33], multi-drug and toxin extrusion (MATE) family [55], small multi-drug resistance (SMR), and sugars will eventually be exported transporters (SWEETs) [17]. The rocker-switch mechanism involves symmetrical helix bundles forming a V-shaped architecture, with the two symmetrical domains undergoing ~30° movements to alternate between four conformations: outward-open, outward-occluded, inward-occluded, and inward-open.

Members of the APC (Amino Acid-Polyamine-Organocation Transporter) superfamily utilize the rocking-bundle mechanism exemplified by the LeuT transporter. LeuT, from the thermophile *Aquifex aeolicus* [73], is a Na+-coupled symporter belonging to the neurotransmitter: Na+ symporter superfamily (NSS) and was the first member of the APC superfamily to be structurally characterized. LeuT has a K-shaped architecture that involves the movement of a pair of discontinuous helices to open and close the internal and external gates. Dozens of other families including the Sodium Solute Symporter (SSS), Cation-Chloride Cotransporter (CCC), and others [3], have been found to share similar architectures known commonly as the ‘LeuT-fold.'

1.2.1 Alternating access mechanism in the LeuT-fold class of transporters

LeuT has been extensively studied, and its structures have provided a framework for understanding the basic architecture and transport mechanism of LeuT-fold transporters, including CCCs. As the structural information of CCCs was not available at the time of initial studies, work on LeuT laid the foundation for understanding the mechanism of transport in this class of transporters.

The LeuT-fold class of transporters consists of two pseudo-symmetric bundles made up of transmembrane helices 1-5 and 6-10, with TM11 and 12 residing outside the symmetric domains. TM1 and 6 are discontinuous and are organized into two parts: a and b (1a, 1b, 6a, and 6b) (Fig. 2D) [53]. TM1b and TM6a together form the extracellular gates, while TM1a and 6b form the cytosolic gates (Fig. 2A). The first LeuT structure was solved in the outward-occluded conformation (Fig. 2B), revealing a binding pocket sealed by residue F253 and containing a bound leucine along with two Na+ ions [73]. In the outward-open structure, the extracellular gate is fully open, and two Na+ ions are bound with no substrate. The inward-open structure revealed an open cytosolic gate by the movement of TM1a ~45° outward toward the membrane [32] (Fig. 2A), facilitating access to the substrate binding pocket from the cytosolic end. The movement of TM1a likely triggers a cascade of structural rearrangements that promotes extracellular gate closure [32]. The LeuT inward-occluded conformation has not been observed, but structural work on homologs ApcT [60] and MhsT [36] suggests that gating in this superfamily involves breaking and forming salt bridges at the intra- and extra-cellular gates, and a LeuT inward-occluded structure likely involves the closure of the extracellular gate and a subtle movement of TM1a (Fig. 2C).

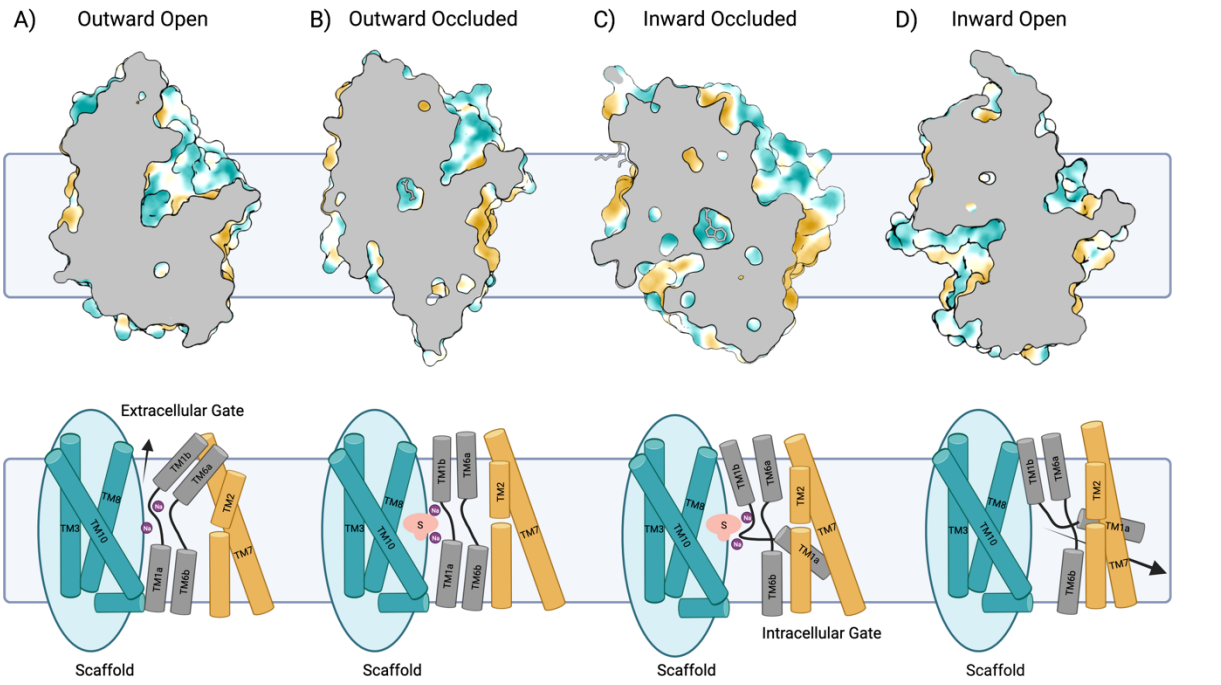

Created with BioRender.com

Figure 2: Transport cycle of LeuT-fold transporters.
This mechanism involves the rocking bundle alternating access model, with LeuT in the Outward open, Outward occluded, and Inward open states (A, B, D). The MhsT transporter is included in the Inward Occluded state (C). In the outward open state, Na+ and substrate (S) bind to the transporter, which then undergoes a conformational change to the outward occluded state, trapping the substrate and retaining the Na+ ion. The transporter then shifts to the inward open state, releasing the substrate into the intracellular space while the Na+ ion is released into the transporter. Finally, the inward occluded state is achieved, where the Na+ ion is trapped while the substrate binding site is inaccessible. Figure adapted from Drew D, Boudker O. 2016.

1.3 The SLC12 Family of Cation-Chloride Cotransporters

The SLC superfamily in humans includes 458 transport proteins across 65 families, with the SLC12 family consisting of nine genes that encode electroneutral, secondary-active CCCs. These proteins facilitate the symport of Na+ or K+ with Cl- for various physiological processes [54]. The SLC12 family can be further divided into four subfamilies: Na+-K+-2Cl- cotransporters (NKCCs, SLC12A1-A2), Na+-Cl- cotransporters (NCC, SLC12A3), K+-Cl-cotransporters (KCC1-4, SLCA4-A7), a nicotinamide mononucleotide (NMN) transporter (CCC9, SLC12A8) [23] and a CCC interacting protein (CIP1, SLC12A9). Prior to my work, no full-length CCC structures had been obtained, so information on structural organization relied on biochemical and computational analyses [24]. Hydrophobicity plots initially predicted 10-13 transmembrane domains, but *in vivo* and *in vitro* analyses with truncated mutants showed that NKCC1 has 12 TMs and intracellular N and C termini [21, 22].

Mutagenesis and structure-based homology experiments in NKCC1 using the APC superfamily members AdiC and ApcT have identified several residues on one face of TM3, which contains several highly conserved residues, as serving a role in the translocation pathway. Mutations in TM3 affected translocation rate, apparent ion affinities, and loop diuretic affinities. In AdiC, TM11 and TM12 form the dimerization interface. Met-382 was predicted to be part of the extracellular gate that promotes the occluded state. An NKCC1 homology model derived from AdiC and ApcT suggests that TMs 1, 3, 6, 8, and 10 make up the translocation pathway. Interestingly, the authors expressed skepticism about the likelihood of the "rocking bundle" gating mechanism for the CCCs transport cycle due to the CCCs turnover rate. NKCC1, which has a turnover rate >20-fold greater than LeuT, SERT, SGLT1, and Gly1, was theorized to undergo more subtle conformational changes during the transport cycle than LeuT [64].

1.3.1 CCCs Large Extracellular Loop

Although KCCs and NKCCs share structural homology, they differ in the placement of their long extracellular loop (LEL). In KCCs, the LEL is located between TM5 and TM6, while in NKCCs, it is between TM7 and TM8. The LEL is functionally and structurally diverse, containing several N-linked glycosylation sites that confirm its extracellular location [28, 48, 72]. Mutations of these glycosylation sites in NCC and NKCC2 have been shown to reduce surface expression [28, 48] while eliminating all three sites in flounder NCC decreased transport by 50% [43]. In KCC4, mutations of the LEL cysteines led to transporter accumulation in the endoplasmic reticulum and reduced transporter stability. Mutations of the cysteines in *Rn*KCC2 rendered the transporter inactive, but the analogous mutations in *Mm*KCC4 had no effect on activity. Chimeras of KCC2 with KCC4 LEL do not alter activity [24], but KCC4 is non-functional when KCC2 LEL is introduced. These experiments suggest that the cysteines play a crucial role in KCCs gating, likely by stabilizing the structure of the LEL [72].

1.3.2 CCCs Oligomerization

Investigations into the native oligomeric state of CCCs have focused on identifying regions responsible for mediating oligomerization through biochemical and functional interaction studies. Oligomerization can have important functional implications for CCCs. For example, it has been suggested that dimerization of KCC2 may be important for its function in regulating chloride ion transport in neurons. Disruption of the dimerization interface of KCC2 can result in decreased transport activity and impaired neuronal function.

Much of the research on the molecular interactions that underlie dimerization has been conducted on NKCC1, which has been found to exclusively exist as a dimer and can withstand membrane solubilization with mild detergents [42]. Homodimers have also been observed in NKCC2, NCC, and the KCCs. Truncating 20kDa out of the first 28kDa of the N-terminal

domain revealed that the N-terminal domain in NKCC1 does not play a role in dimerization. Subsequent work replacing 50kDa of the NKCC1 C-terminal domain with that of other non-NKCC1 homologs (NKCC1, NCC, or CIP) revealed that aa 751-998 of the CTD contained homolog-specific residues necessary for dimerization. NKCC1 could not dimerize with NKCC2 or CIP and had weak interactions with NCC [49]. Further research using chimeric approaches revealed four regions within aa 751-998 that were important for dimerization (806-814, 842-912, 825-841, and 815-825), and mutagenesis between residues 806-814 impaired dimerization significantly [50].

The involvement of the CTD in oligomerization is supported by structural studies of the archean *Methanosarcina acetivorans* CCC, where the CTD forms a dimeric, compact trapezoid-shaped structure with a poorly conserved protein interaction interface predicted to aid in dimer stability. The dimer interface is hydrophilic and makes up 6% of the total molecule surface [69]. Mapping *Rn*NKCC1 aa residues 806-814 onto the archean CCC showed that the interacting region was located near the dimerization interface [50].

Oligomerization of cation chloride cotransporters (CCCs) is suggested to also be mediated by transmembrane domain interactions. When an inactive KCC1 was heterologously co-expressed with other KCC family members, a dose-dependent reduction in transport activity was observed [7], indicating the likely role of transmembrane domains in dimerization. Deletion of the N- or C-termini in KCC1 did not affect oligomerization, further supporting the importance of transmembrane domains in dimerization [8].

In addition, specific transmembrane domains have been identified as dimeric interfaces in some LeuT-fold transporters such as TM11 and 12 in the AdiC transporter. In yeast two-hybrid experiments that tested the dimerization of full-length KCCs C-terminal domains, KCC2, and KCC4 dimerize while KCC1 and KCC3 did not interact [61]. The deletion of the last 28 amino acids of KCC2 impaired oligomerization and increased the proportion of monomers [70]. It has been proposed that a combination of C-terminal domains and transmembrane helices mediate oligomerization, however, dimerization may differ slightly among CCCs [61].

1.4 Principles of Cell Volume Regulation

Animal cells regulate their volume by controlling the movement of ions and water across the cell membrane in response to changes in solute concentration. Osmosis is the passive diffusion of water across a semipermeable membrane from an area of low solute concentration to an area of high solute concentration until equilibrium is reached. The plasma membrane allows water to move across freely, opposed only by a hydrostatic force known as osmotic pressure. The osmotic pressure formula, $\pi = nRT/V$, was developed by Jacobus H. van't Hoff, who postulated that solutes in dilute solutions obey the ideal gas laws. Due to the high proportion of negatively

charged membrane-impermeant macromolecules (i.e. proteins, DNA, RNA) in the cytoplasm, cells are prone to swelling, a phenomenon known as Donnan swelling. Unlike bacteria and plant cells, which have cell walls to provide hydrostatic pressure to oppose changes in cell volume, animal cells have evolved mechanisms to regulate their volume by manipulating ionic gradients.

The regulation of animal cell volume involves the Double Donnan effect, which results from the combined effects of fixed intracellular anions and the sodium pump's ATPase. The first Donnan effect is caused by the excess of impermeant negatively charged macromolecules such as proteins, RNA, and DNA within the cell, which causes a large driving force for cations, such as Na+, to enter the cell. At steady state, the system reaches charge balance but not osmotic equilibrium without bursting due to the excess of osmotic material within the cell. The second Donnan effect is generated by the Na+/K+-ATPase pump, which uses ATP energy to move three Na+ ions out of the cell in exchange for two K+ ions. This immobilizes Na+ externally, achieves a high internal [K+], and causes the cell to shrink by driving water out. In a typical cell, where both effects are present, the cell can reach osmotic equilibrium, set a membrane potential, and establish ionic gradients using energy [41, 65, 67].

1.4.1 Regulatory Volume Increase (RVI)

Regulatory Volume Increase (RVI) is essential for restoring normal volume after hyperosmotic cell shrinkage stress. RVI involves several mechanisms, including the activation of ion and osmolyte transporters and ion channels. Specifically, transporters such as the Na+/H+ exchanger (NHE), the Cl--HCO3- anion exchanger (AE), and the Na+/K+/2Cl--cotransporter (NKCC) become activated, resulting in a net gain of Na+ and HCO_3- and efflux of H+ and Cl- ions. This influx is driven by the concentration gradient established by the Na+/K+ ATPase pump. In addition, ion channels like the volume-regulated anion channel (VRAC) and Ca2+-activated K+ channels (KCa) allow the efflux of Cl- and organic anions, and KCa facilitates the efflux of K+. Osmolyte transporters such as the taurine transporter (TauT) lead to the accumulation of osmolytes that help restore cell volume. The net movement of ions and water increases the intracellular osmolarity, driving the movement of water into the cell and recovering the original cell volume [27].

1.4.2 Regulatory Volume Decrease (RVD)

Regulatory Volume Decrease (RVD) occurs when cells are exposed to a hypotonic environment, leading to cell swelling. To maintain cell homeostasis and prevent excessive swelling, various transporters and ion channels are activated to facilitate the efflux of ions and osmolytes, resulting in the loss of intracellular solutes and water. The main transporters and channels involved in RVD are CCCs and the Volume Regulated Anion channel (VRAC). The inactivation of NKCCs and activation of KCCs and VRACs leads to the efflux of Cl- ions. This results in an increase in

intracellular positive charge, driving the efflux of K^+ ions and contributing to further decrease in cell volume and the release of intracellular osmolytes and organic anions.

1.4.3 Regulation of Cation Chloride Cotransporters During RVI and RVD

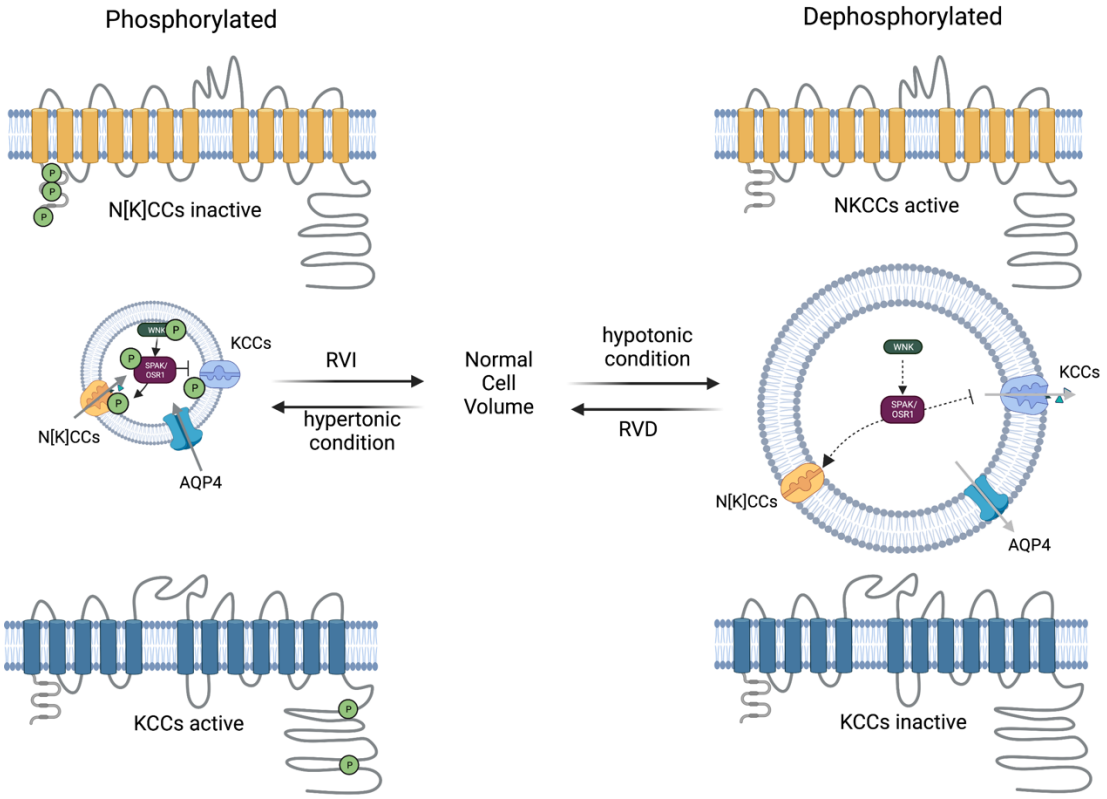

Created with BioRender.com

Figure 3: Role of CCCs in cell osmoregulation.
Cells can adjust their volume in response to changes in fluid concentration, through regulatory volume increase (RVI) or regulatory volume decrease (RVD). Cation-chloride cotransporters (CCCs) are key regulators of this process, and their activation is controlled by the WNK-SPAK/OSR1 pathway depending on the type of response needed. Under hypertonic conditions, RVI restores cell volume by activating NKCC1 and inhibiting KCC through CCC phosphorylation. Under hypotonic conditions, RVD decreases cell volume by dephosphorylating NKCC1 and KCC, leading to KCC3 stimulation and NKCC1 inhibition, and efflux of K+ and Cl- along with water. NKCC1, K^+-Cl^- cotransporters; KCC3, K^+-Cl^- cotransporter 3; WNK, with-no-lysine kinase; SPAK, STE20/SPS1-related proline/alanine rich kinase; OSR1, oxidative stress response kinase; AQP4, aquaporin. Parts of the figure elements were adapted from Alessi et al 2014 and Josiah 2021.

Phosphorylation and dephosphorylation mechanisms modulate CCCs activity and ability to respond to changes in cell volume and intracellular chloride concentration $[Cl^-]_i$ (Figure 3) [14]. KCC1-KCC4 were originally studied in red blood cells where they were found to regulate red blood cell volume [39]. This early work observed that phosphorylation of key serine/threonine residues on NKCCs/NCCs and KCCs have reciprocal effects on transport activity. When cells shrink or have a decrease in [Cl-]i, CCC phosphorylation activates NKCCs/NCCs and inactivates

KCCs. Conversely, when cells swell or have an increase in [Cl-]i, CCC dephosphorylation inhibits NKCCs/NCCs and activates KCCs (Fig. 3).

Intracellular chloride depletion is communicated through a complex cascade of kinases and phosphatases to CCCs [4]. SPS1-related proline/alanine-rich kinase/oxidative stress-responsive kinase 1 (SPAK/OSR1) is one of the kinases that directly phosphorylate CCCs. The with no lysine (WNK) kinases are located upstream of SPAK/OSR1 and are capable of detecting changes in cell volume and intracellular chloride concentrations [75]. Different WNK isoforms have varying sensitivities to intracellular chloride levels, with WNK4 being the most sensitive to [Cl-]i followed by WNK1 [56].

1.5 Physiological roles of cation chloride cotransporters

CCC transporters are expressed in various tissues throughout the body and regulate a wide range of physiological and pathophysiological processes, such as cardiovascular and brain pathophysiology, blood pressure regulation, tumoral diseases, and hearing. In the brain, CCCs primarily regulate the concentration of chloride ions in neurons and glial cells, maintaining inhibitory tone in the central nervous system through their involvement in the GABAergic and glycinergic systems. KCC2, expressed mainly in neurons, is also critical for the development and maturation of the nervous system. In the kidney, CCCs play a vital role in reabsorbing ions and water from the tubular fluid, and NKCC2 is critical in generating the corticomedullary osmotic gradient required for the concentration and dilution of urine. In the gastrointestinal tract, CCCs regulate ion and fluid transport across the epithelial cells lining the gut, and NKCC1, expressed in enterocytes, is crucial in absorbing nutrients and electrolytes from the lumen of the gut.

1.5.1 The role of KCC4 in the physiology of hearing

The inner ear's cochlea is responsible for converting sound waves into neural signals that the brain can interpret as sound. This process relies on the proper function of specialized cells within the cochlea that respond to mechanical vibrations produced by sound waves. These cells are sensitive to the ionic composition of the fluid surrounding them. Perilymph and endolymph are two extracellular fluids that play important roles in the normal function of the inner ear. Perilymph surrounds the endolymphatic duct and is rich in sodium ions, while endolymph is located within the cochlear duct and is rich in potassium ions.

The separation of these two fluids is critical for the normal function of the cochlea. For example, the hair cells that detect sound waves rely on a high concentration of potassium ions in the endolymph for their proper function. Any mixing of the endolymph with perilymph, which has a lower potassium concentration, can reduce the driving force for potassium ions and impair the

function of the hair cells. Similarly, any influx of sodium ions from the perilymph into the endolymph can also disrupt the balance of ions and impair the function of the inner ear.

The Endolymph is composed of an unusually high concentration of K+ (157mM), low amounts of Na+ (2mM) and Ca2+(20uM). This specialized composition and its physical separation generate a positive potential called the endocochlear potential (EP), critical for hair cell mechanotransduction. The perilymph, on the other hand, is more typical in composition of other extracellular fluids such as cerebral spinal fluid (4mM K+, 148mM Na+, and 1.3mM Ca2+) and submerges the basolateral side of hair cells. The electrochemical gradient across the apical and basal regions of hair cells is essential for hair cell function and consequently audition[45]. During audition, mechanosensitive channels on the stereocilia of hair cells open, allowing K+ ions to travel down their electrochemical gradient from the endolymph and into the cytosol. K+ ions then exit through the potassium voltage-gated channel subfamily Q member 4 (KCNQ4) channel located on the basolateral membrane into perilymph where it is readily siphoned away by KCC4 expressed on supporting cells[44, 68, 76].

Deiters' cells surround OHCs and are connected via gap junctions to epithelial cells that line the base of the organ of Corti. KCC4 participates in the K+ recycling pathway which serves to shuttle K+ back into the endolymph after hair cell activation. Evidence of this function is demonstrated by the KCC4-/- mouse phenotype which exhibits hearing loss due to the rapid degeneration of their hair cells after the beginning of hearing[6]. This phenotype suggests KCC4's importance in the survival and maintenance of OHCs and supporting cells in the organ of Corti. KCC4 achieves this function by sequestering extracellular K+ from the OHC-Deiters cell cleft. If left to accumulate, osmotic stress or membrane depolarization on OHCs result in cell death and therefore hearing loss. Expanding our structural and mechanistic understanding of KCC4 and other CCCs will enable us to pharmacologically modulate the activity of these transporters, allowing for potential therapeutic treatments of progressive hearing loss, renal acidosis, and other diseases associated with ionic imbalances.

1.6 References

1. Acton, B. A., Mahadevan, V., Mercado, A., Uvarov, P., Ding, Y., Pressey, J., et al. (2012). Hyperpolarizing GABAergic transmission requires the KCC2 C-terminal ISO domain. *J. Neurosci.* 32, 8746–8751. doi: 10.1523/JNEUROSCI.6089-11.2012
2. Adragna, N. C., & Lauf, P. K. (2015). Regulation of the NKCC2 ion cotransporter by SPAK-OSR1-dependent and -independent pathways. Comprehensive Physiology, 5(1), 43-60. https://www.ncbi.nlm.nih.gov/pubmed/25589268
3. Alamo, Diego del, et al. "Principles of Alternating Access in LeuT-Fold Transporters: Commonalities and Divergences." *Journal of Molecular Biology*, Academic Press, 16 July 2022, www.sciencedirect.com/science/article/pii/S0022283622003485.
4. Alessi, D. R., Zhang, J., Khanna, A., Hochdörfer, T., Shang, Y., and Kahle, K. T. (2014). The WNK-SPAK/OSR1 pathway: master regulator of cation-chloride cotransporters. Sci. Signal. 7:re3. doi: 10.1126/scisignal.2005365
5. Barmeyer, C., Harren, M., Schmitz, H., Heinzel-Pleines, U., Mally, S., Pauli, B. U., ... & Fromm, M. (2004). Mechanisms of diarrhea in the interleukin-2-deficient mouse model of colonic inflammation. American Journal of Physiology-Gastrointestinal and Liver Physiology, 286(2), G244-G252. https://www.ncbi.nlm.nih.gov/pubmed/14656721
6. Boettger, T., Hübner, C., Maier, H., Rust, M., Beck, F. and Jentsch, T. (2002). Deafness and renal tubular acidosis in mice lacking the K-Cl co-transporter Kcc4. *Nature*, 416(6883), pp.874-878.
7. Casula, S., Shmukler, B. E., Wihelm, S., Stuart-Tilley, A. K., Su, W., Chernova, M., et al. (2001). A dominant negative mutant of the KCC1 K-Cl cotransporter. J. Biol. Chem. 276, 41870–41878. doi: 10.1074/jbc.m107155200
8. Casula, S., Zolotarev, A. S., Stuart-Tilley, A. K., Wilhelm, S., Shmukler, B. E., Brugnara, C., et al. (2009). Chemical cross-linking studies with the mouse KCC1 K-Cl cotransporter. Blood Cells Mol. Dis. 42, 233–240. doi: 10.1016/j.bcmd.2009.01.021
9. Chi, Gamma. "Phospho-Regulation, Nucleotide Binding and Ion Access Control in Potassium-Chloride Cotransporters." *The EMBO Journal*, U.S. National Library of Medicine, 25 May 2021, https://pubmed.ncbi.nlm.nih.gov/34031912/.
10. Czuba LC, Hillgren KM, Swaan PW. Post-translational modifications of transporters. Pharmacol Ther. 2018 Dec;192:88-99. doi: 10.1016/j.pharmthera.2018.06.013. Epub 2018 Jun 30. PMID: 29966598; PMCID: PMC626385
11. Di Fulvio, M., and Alvarez-Leefmans, F. J. (2009). "The NKCC and NCC genes: an in silico view," in *Physiology and Pathology of Chloride Transporters and Channels in the Nervous System* (London: Academic Press), 169–208.
12. Delpire, E., & Gagnon, K. B. (2018). Na-K-2Cl cotransporter (NKCC) physiological function, activation and inhibition. In Comprehensive Physiology (pp. 611-634). John Wiley & Sons, Inc.. https://www.ncbi.nlm.nih.gov/pmc/articles/PMC6491325/
13. Delpire E, Gagnon KB. Water Homeostasis and Cell Volume Maintenance and Regulation. Curr Top Membr. 2018;81:3-52. doi: 10.1016/bs.ctm.2018.08.001. Epub 2018 Aug 27. PMID: 30243436; PMCID: PMC6457474.
14. Delpire E, Gagnon KB. SPAK and OSR1: STE20 kinases involved in the regulation of ion homoeostasis and volume control in mammalian cells. Biochem J. 2018 Nov 20;475(22):3361-3378. doi: 10.1042/BCJ20180334. PMID: 30459212.

15. Drew D, Boudker O. Shared Molecular Mechanisms of Membrane Transporters. Annu Rev Biochem. 2016 Jun 2;85:543-72. doi: 10.1146/annurev-biochem-060815-014520. Epub 2016 Mar 21. PMID: 27023848.
16. Fang, Y., Jayaram, H., Shane, T., Kolmakova-Partensky, L., Wu, F., Williams, C., et al. (2009). Structure of a prokaryotic virtual proton pump at 3.2 Å resolution. *Nature* 460, 1040–1043. doi: 10.1038/nature08201
17. Feng L, Frommer WB. Structure and function of SemiSWEET and SWEET sugar transporters. Trends Biochem Sci. 2015 Aug;40(8):480-6. doi: 10.1016/j.tibs.2015.05.005. Epub 2015 Jun 9. PMID: 26071195.
18. Fugelli K. Regulation of cell volume in flounder (Pleuronectes flesus) erythrocytes accompanying a decrease in plasma osmolarity,Comparative Biochemistry and Physiology, Volume 22, Issue 1, 1967, Pages 253-260, ISSN 0010-406X, https://doi.org/10.1016/0010-406X(67)90185-5 (https://www.sciencedirect.com/science/article/pii/0010406X67901855)
19. Gamba, G. (2005). Molecular physiology and pathophysiology of electroneutral cation-chloride cotransporter. *Physiol. Rev.* 85, 423–493. doi: 10.1152/physrev.00011.2004
20. Gamba, G. (2012). Molecular physiology and pathophysiology of electroneutral cation-chloride cotransporters. Physiological reviews, 92(1), 21-76. https://www.ncbi.nlm.nih.gov/pubmed/22298651
21. Gerelsaikhan, T., and Turner, R. J. (2000). Transmembrane topology of the secretory Na+-K+-2Cl− cotransporter NKCC1 studied by in vitro translation. J. Biol. Chem. 275, 40471–40477. doi: 10.1074/jbc.m007751200
22. Gerelsaikhan, T., Parvin, M. N., and Turner, R. J. (2006). Biogenesis and topology of the secretory Na+-K+-2Cl− cotransporter (NKCC1) studied in intact mammalian cells. Biochemistry 45, 12060–12067. doi: 10.1021/bi061126x
23. Grozio, Alessia, et al. "Slc12a8 Is a Nicotinamide Mononucleotide Transporter." *Nature News*, Nature Publishing Group, 7 Jan. 2019, www.nature.com/articles/s42255-018-0009-4.
24. Hartmann, A.-M., Wenz, M., Mercado, A., Störger, C., Mount, D. B., Friauf, E., et al. (2010). Differences in the large extracellular loop between the K+-Cl− cotransporters KCC2 and KCC4. *J. Biol. Chem.* 285, 23994–24002. doi: 10.1074/jbc.m110.144063
25. Hartmann A.-M., David Tesch, Hans Gerd Nothwang, Olaf R.P. Bininda-Emonds, Evolution of the Cation Chloride Cotransporter Family: Ancient Origins, Gene Losses, and Subfunctionalization through Duplication, *Molecular Biology and Evolution*, Volume 31, Issue 2, February 2014, Pages 434–447, https://doi.org/10.1093/molbev/mst225
26. Hediger MA, Clémençon B, Burrier RE, Bruford EA. The ABCs of membrane transporters in health and disease (SLC series): introduction. Mol Aspects Med. 2013 Apr-Jun;34(2-3):95-107. doi: 10.1016/j.mam.2012.12.009. PMID: 23506860; PMCID: PMC3853582.
27. de Los Heros P, D. Pacheco-Alvarez, G. Gamba. Role of WNK kinases in the modulation of cell volume. Curr. Top. Membr., 81 (2018), pp. 207-235
28. Hoover, R. S., Poch, E., Monroy, A., Vázquez, N., Nishio, T., Gamba, G., et al. (2003). N-Glycosylation at two sites critically alters thiazide binding and activity of the rat thiazide-sensitive Na+:Cl− cotransporter. *J. Am. Soc. Nephrol.* 14, 217–282. doi: 10.1097/01.asn.0000043903.93452.d0

29. International Transporter Consortium; Giacomini KM, Huang SM, Tweedie DJ, Benet LZ, Brouwer KL, Chu X, Dahlin A, Evers R, Fischer V, Hillgren KM, Hoffmaster KA, Ishikawa T, Keppler D, Kim RB, Lee CA, Niemi M, Polli JW, Sugiyama Y, Swaan PW, Ware JA, Wright SH, Yee SW, Zamek-Gliszczynski MJ, Zhang L. Membrane transporters in drug development. Nat Rev Drug Discov. 2010 Mar;9(3):215-36. doi: 10.1038/nrd3028. PMID: 20190787; PMCID: PMC3326076.
30. Kahle, K. T., & Rinehart, J. (2010). Physiology of the choroid plexus and cerebrospinal fluid production. In Handbook of clinical neurology (Vol. 97, pp. 25-37). Elsevier. https://www.ncbi.nlm.nih.gov/pmc/articles/PMC3680698/
31. Kazmier, K., Claxton, D. P., & Mchaourab, H. S. "Alternating access mechanisms of LeuT-fold transporters: trailblazing towards the promised energy landscapes." Current Opinion in Structural Biology, vol. 45, 2017, pp. 100-108. doi: 10.1016/j.sbi.2016.12.006. PMID: 28040635; PMCID: PMC5491374.
32. Krishnamurthy, H., & Gouaux, E. "X-ray structures of LeuT in substrate-free outward-open and apo inward-open states." Nature, vol. 481, no. 7382, 2012, pp. 469-474. doi: 10.1038/nature10737. PMID: 22230955; PMCID: PMC3306218.
33. Kumar, H., Kasho, V., Smirnova, I., Finer-Moore, J. S., Kaback, H. R., & Stroud, R. M. "Structure of sugar-bound LacY." Proceedings of the National Academy of Sciences, vol. 111, no. 5, 2014, pp. 1784-1788.
34. Kyte, J., & Doolittle, R. F. "A simple method for displaying the hydropathic character of a protein." Journal of Molecular Biology, vol. 157, no. 1, 1982, pp. 105-132. doi: 10.1016/0022-2836(82)90515-0.
35. Lin, L., Yee, S. W., Kim, R. B., & Giacomini, K. M. "SLC transporters as therapeutic targets: emerging opportunities." Nature Reviews Drug Discovery, vol. 14, no. 8, 2015, pp. 543-560. doi: 10.1038/nrd4626. PMID: 26111766; PMCID: PMC4698371.
36. Malinauskaite, L., Quick, M., Reinhard, L., Lyons, J. A., Yano, H., Javitch, J. A., et al. "A mechanism for intracellular release of Na+ by neurotransmitter/sodium symporters." Nature Structural & Molecular Biology, vol. 21, no. 10, 2014, pp. 1006-1012. doi: 10.1038/nsmb.2907.
37. Majumder, P., Mallela, A. K., & Penmatsa, A. "Transporters through the looking glass. An insight into the mechanisms of ion-coupled transport and methods that help reveal them." Journal of Indian Institute of Science, vol. 98, no. 3, 2018, pp. 283-300.
38. Medina, I., Friedel, P., Rivera, C., Kahle, K. T., Kourdougli, N., & Uvarov, P. (2017). Current view on the functional regulation of the neuronal K+-Cl− cotransporter KCC2. Frontiers in cellular neuroscience, 11, 432. https://www.ncbi.nlm.nih.gov/pmc/articles/PMC5768566/
39. Mercado A, Broumand V. Cation-Chloride Cotransporters in Red Blood Cells. Int J Mol Sci. 2020 Jan 3;21(1):354. doi: 10.3390/ijms21010354. PMID: 31947898; PMCID: PMC6981792.
40. Meor Azlan, N. F., & Zhang, J. "Role of the Cation-Chloride-Cotransporters in Cardiovascular Disease." Cells, vol. 9, no. 10, 2020, p. 2293. doi: 10.3390/cells9102293. PMID: 33066544; PMCID: PMC7602155.
41. Mongin, A. A. "Characteristics of voltage-gated chloride channels in Xenopus oocytes." Pflügers Archiv-European Journal of Physiology, vol. 455, no. 5, 2008

42. Moore-Hoon, M. L., and Turner, R. J. "The structural unit of the secretory Na+-K+-2Cl− cotransporter (NKCC1) is a homodimer." Biochemistry, vol. 39, no. 13, 2000, pp. 3718-3724. doi: 10.1021/bi992301v.
43. Moreno, E., Crisóbal, P. S., Rivera, C., Vázquez, N., Bobadilla, N. A., and Gamba, G. "Affinity-defining domains in the Na-Cl cotransporter: a different location for Cl− and thiazide binding." J. Biol. Chem., vol. 281, no. 25, 2006, pp. 17266-17275. doi: 10.1074/jbc.m602614200.
44. Nickel, R. and Forge, A. (2008). Gap junctions and connexins in the inner ear: their roles in homeostasis and deafness. *Current Opinion in Otolaryngology & Head and Neck Surgery*, 16(5), pp.452-457
45. Nin, F., Hibino, H., Doi, K., Suzuki, T., Hisa, Y. and Kurachi, Y. (2008). The endocochlear potential depends on two K+ diffusion potentials and an electrical barrier in the stria vascularis of the inner ear. *Proceedings of the National Academy of Sciences*, 105(5), pp.1751-1756
46. Pacheco-Alvarez, D. "Regulation of ion channels by intracellular trafficking: Insights from the calcium-activated chloride channel Ano1/TMEM16A." Channels (Austin, Tex.), vol. 14, no. 1, 2020, pp. 88-97. doi: 10.1080/19336950.2019.1708507.
47. Pacheco-Alvarez D, Gamba G. The role of the With-No-Lysine Kinase 1/SPAK Complex in Renal Physiology and Blood Pressure Regulation. Front Physiol. 2020 Dec 10;11:606831. doi: 10.3389/fphys.2020.606831. PMID: 33390901; PMCID: PMC7767359.
48. Paredes, A., Plata, C., Rivera, M., Moreno, E., Vázquez, N., Muñoz-Clares, R., et al. "Activity of the renal Na+-K+-2Cl− cotransporter is reduced by mutagenesis of N-glycosylation sites: role for protein surface charge in Cl− transport." Am. J. Physiol. Renal Physiol., vol. 290, no. 5, 2006, pp. F1094-F1102. doi: 10.1152/ajprenal.00071.2005.
49. Parvin, M. N., Gerelsaikhan, T., and Turner, R. J. "Regions in the cytosolic C-Terminus of the secretory Na+-K+-2Cl− cotransporter NKCC1 are required for its homodimerization." Biochemistry, vol. 46, no. 32, 2007, pp. 9630-9637. doi: 10.1021/bi700881a.
50. Parvin, M. N., and Turner, R. J. "Identification of key residues involved in the dimerization of the secretory Na+-K+-2Cl− cotransporter NKCC1." Biochemistry, vol. 50, no. 42, 2011, pp. 9857-9864. doi: 10.1021/bi201498y.
51. Payne, J. A., Stevenson, T. J., and Donaldson, L. F. "Molecular characterization of a putative K-Cl cotransporter in rat brain. A neuronal-specific isoform." J. Biol. Chem., vol. 271, no. 27, 1996, pp. 16245-16252. doi: 10.1074/jbc.271.27.16245.
52. Payne, J. A., Forbush, B., & Kavanaugh, M. P. (1996). Sodium-coupled chloride transporters in the nervous system. The Journal of experimental biology, 199(Pt 2), 263-276. https://www.ncbi.nlm.nih.gov/pubmed/9319420
53. Penmatsa A, Gouaux E. "How LeuT shapes our understanding of the mechanisms of sodium-coupled neurotransmitter transporters." J Physiol, vol. 592, no. 5, 2014, pp. 863-869. doi: 10.1113/jphysiol.201
54. Pizzagalli, MD, Bensimon, A., & Superti-Furga, G. "A guide to plasma membrane solute carrier proteins." FEBS J., vol. 288, no. 9, May 2021, pp. 2784-2835. doi: 10.1111/febs.15531. Epub 2020 Sep 18. PMID: 32810346; PMCID: PMC8246967.

55. Radchenko, M., Symersky, J., Nie, R., Lu, M., and Vaughan, R. (2015). Structural basis for the blockade of mate multidrug efflux pumps. Nature Communications, 6, 8163. doi: 10.1038/ncomms9163
56. Richardson C, Alessi DR. The Regulation of Salt Transport and Blood Pressure by the WNK-SPAK/OSR1 Signalling Pathway. J Cardiovasc Dev Dis. 2021 Mar 5;8(3):28. doi: 10.3390/jcdd8030028. PMID: 33807955; PMCID: PMC7994476.
57. Rivera, C., Voipio, J., Payne, J. *et al.* The K^+/Cl^- co-transporter KCC2 renders GABA hyperpolarizing during neuronal maturation. *Nature* **397**, 251–255 (1999). https://doi.org/10.1038/16697
58. Rosenbaek, L. L., & Rizzo, F. (2017). A clinical guide to inherited disorders of renal electrolyte transport. Nature Reviews Nephrology, 13(9), 549-563. https://www.ncbi.nlm.nih.gov/pubmed/28584229
59. Schlingmann, K. P., & Konrad, M. (2018). Diagnosis and treatment of Bartter and Gitelman syndromes. In Comprehensive Physiology (pp. 917-940). John Wiley & Sons, Inc.. https://www.ncbi.nlm.nih.gov/pubmed/29687925
60. Shaffer, P. L., Goehring, A., Shankaranarayanan, A., & Gouaux, E. (2009). Structure and mechanism of a Na+ independent amino acid transporter. Science, 325(5943), 1010–1014. doi: 10.1126/science.1176088
61. Simard, C. F., Brunet, G., Daigle, N. D., Montminy, V., Caron, L., & Isenring, P. (2004). Self-interacting domains in the C terminus of a cation-Cl− cotransporter described for the first time. Journal of Biological Chemistry, 279(40), 40769–40777. doi: 10.1074/jbc.M406458200
62. Simard, C. F., Bergeron, M. J., Frenette-Cotton, R., Carpentier, G. A., Pelchat, M.-E., Caron, L., et al. (2007). Homooligomeric and heterooligomeric associations between K+-Cl− cotransporter isoforms and between K+-Cl− and Na+-K+-Cl− cotransporter. Journal of Biological Chemistry, 282(25), 18083–18093. doi: 10.1074/jbc.M607811200
63. Singh, A. K., & Seth, P. (2010). Regulatory mechanisms of KCC2 expression in neurons. Frontiers in cellular neuroscience, 4, 26. https://www.ncbi.nlm.nih.gov/pmc/articles/PMC2901651/
64. Somasekharan, S., Tanis, J. E., Kim, J. Y., Oh, B. C., and Gagnon, K. B. (2012). Loop diuretic and ion-binding residues revealed by scanning mutagenesis of transmembrane helix 3 (TM3) of Na-K-Cl cotransporter (NKCC1). Journal of Biological Chemistry, 287(22), 18190–18199. doi: 10.1074/jbc.M111.323105
65. Stein, W. D. (2004). The movement of molecules across cell membranes. New York: Academic Press.
66. Tao, Y., Cheung, L., Li, S., Eom, J. S., Chen, L., Xu, Y., et al. (2015). Structure of a eukaryotic sweet transporter in a homotrimeric complex. Nature, 527(7577), 540–544. doi: 10.1038/nature15391
67. Tosteson, D. C., & Hoffman, J. F. (1960). Regulation of cell volume by active cation transport in high and low potassium sheep red cells. Journal of General Physiology, 43(4), 737-752. doi: 10.1085/jgp.43.4.737
68. Wan, G., Corfas, G. and Stone, J. (2013). Inner ear supporting cells: Rethinking the silent majority. *Seminars in Cell & Developmental Biology*, 24(5), pp.448-459.

69. Warmuth, S., Zimmermann, I., & Dutzler, R. (2009). X-ray structure of the C-terminal domain of a prokaryotic cation-chloride cotransporter. Structure, 17(5), 538–546. doi: 10.1016/j.str.2009.02.009
70. Watanabe, M., Wake, H., Moorhouse, A. J., & Nabekura, J. (2009). Clustering of neuronal K+-Cl− cotransporter
71. Weber, M., Hartmann, A.-M., Beyer, T., Ripperger, A., and Nothwang, H. G. "A novel regulatory locus of phosphorylation in the C-terminus of the potassium chloride cotransporter KCC2 that interferes with N-ethylmaleimide or staurosporine mediated activation." Journal of Biological Chemistry, vol. 289, 2014, pp. 18668–18679. doi: 10.1074/jbc.M114.567834.
72. Weng, TY, Chiu, WT, Liu, HS, Cheng, HC, Shen, MR, Mount, DB, and Chou, CY. "Glycosylation regulates the function and membrane localization of KCC4." Biochimica et Biophysica Acta, vol. 1833, no. 5, 2013, pp. 1133-1146. doi: 10.1016/j.bbamcr.2013.01.018. PMID: 23376777.
73. Yamashita, A., Singh, S., Kawate, T. et al. "Crystal structure of a bacterial homologue of Na+/Cl--dependent neurotransmitter transporters." Nature, vol. 437, 2005, pp. 215-223. doi: 10.1038/nature03978.
74. Yan, N. "Structural biology of the major facilitator superfamily transporters." Annual Review of Biophysics, vol. 44, 2015, pp. 257-283.
75. Yang, C. L., & Angell, J. (2021). Cation-Chloride Cotransporters in Health and Disease. Frontiers in cell and developmental biology, 9, 748693. https://doi.org/10.3389/fcell.2021.748693
76. Zdebik, A., Wangemann, P. and Jentsch, T. (2009). Potassium Ion Movement in the Inner Ear: Insights from Genetic Disease and Mouse Models. *Physiology*, 24(5), pp.307-316.
77. Zhao, B., Wong, A. Y., Murshid, A., Bowie, D., Presley, J. F., and Bedford, F. K. "Identification of a novel di-leucine motif mediated K+/Cl− cotransporter KCC2 internalization and is conserved amongst family members." Cellular Signalling, vol. 20, 2008, pp. 1769-1779. doi: 10.1016/j.cellsig.2008.06.011.

Chapter 2: Cryo-EM structure of K+/Cl- co-transporter KCC4 in lipid nanodiscs

This chapter is adapted, with permission, from work previously published: Reid MS, Kern DM, Brohawn SG. Cryo-EM structure of the potassium-chloride cotransporter KCC4 in lipid nanodiscs. Elife. 2020 Apr 14;9:e52505. doi: 10.7554/eLife.52505. PMID: 32286222; PMCID: PMC7200160.

2.1 Introduction

CCCs in mammals include the potassium-chloride cotransporters KCC1-4, the sodium-potassium-chloride cotransporters NKCC1-2, the sodium-chloride cotransporter NCC, and CCC8-9 (Figure 2—figure supplement 1; Arroyo et al., 2013; Marcoux et al., 2017; Gamba, 2005). First characterized as modulators of red blood cell volume (Dunham et al., 1980; Lauf and Theg, 1980), CCCs are now appreciated to play critical roles in cellular volume regulation, modulation of neuronal excitability, renal function, auditory system function, transepithelial transport, and blood pressure regulation (Marcoux et al., 2017; Gamba, 2005; Singhvi et al., 2016). CCCs are targets of drugs including the thiazide and loop diuretics hydrochlorothiazide, furosemide, and bumetanide and their disruption is associated with congenital hydrocephaly, epilepsy, hearing loss, Andermann syndrome, Gitelman syndrome, and Bartter syndrome (Gamba, 2005; Jin et al., 2019; Kahle et al., 2015).

KCCs are important for K^+ and Cl^- homeostasis, including in establishing low neuronal cytoplasmic Cl- concentrations critical for inhibitory neurotransmission, and in volume regulation in many cell types (Marcoux et al., 2017; Bergeron et al., 2003; Mount et al., 1999; Karadsheh et al., 2004). Among KCCs, KCC4 is most strongly activated by cell swelling and high internal [Cl-] and is uniquely active in acidic external environments (Marcoux et al., 2017; Bergeron et al., 2003). KCC4 is expressed in tissues including the heart, nervous system, kidney, and inner ear and mice lacking KCC4 display progressive deafness and renal tubular acidosis (Marcoux et al., 2017; Mount et al., 1999; Karadsheh et al., 2004; Boettger et al., 2002). Hearing loss in these animals is due to disrupted K+ recycling by Dieter's cells in the cochlea and hair cell excitotoxicity, while renal tubular acidosis is due to impaired Cl^- recycling by α-intercalated cells in the kidney distal nephron (Boettger et al., 2002).

CCCs display varied substrate specificity and transport stoichiometry despite sharing a common amino acid-polyamine-organocation (APC) superfamily fold (Payne, 2012; Hartmann and Nothwang, 2014; Shi, 2013). KCCs cotransport K^+:Cl^- in a 1:1 ratio, NKCCs cotransport $1K^+$:$1Na^+$:2Cl-, and NCCs cotransport 1Na+:1Cl-. One consequence of this difference is that under typical conditions (with [K+]in:[K+]out > [Cl-]out:[Cl-]in), transport by KCCs is outwardly directed while transport by NKCCs/NCCs is directed into cells (Marcoux et al., 2017; Gamba, 2005).

CCCs have two distinctive elaborations on the APC fold. First, the scaffold is followed by a C-terminal domain (CTD) important for regulating expression, trafficking, and activity including through phosphorylation or dephosphorylation of CTD sites in response to cell swelling (Rinehart et al., 2009; Bergeron et al., 2009; Frenette-Cotton et al., 2017; Melo et al., 2013). Second, CCCs contain a 'long extracellular loop' with predicted disulfide bonds and glycosylation sites that differs in position and structure between CCCs; it is formed by the region

between TM5-TM6 in KCCs and between TM7-TM8 in NKCCs (Hartmann and Nothwang, 2014; Hartmann et al., 2010).

KCCs are present as monomers and dimers in cells and modulation of quaternary state has been implicated in transporter regulation. A shift from monomeric to dimeric KCC2 during development coincides with an increase in its activity that results in chloride extrusion from neurons (the excitatory-to-inhibitory GABA switch) (Rivera et al., 1999; Blaesse et al., 2006; Puskarjov et al., 2012). Homodimerization is thought to be largely mediated through CTD interactions, as observed in the recent cryo-EM structure of NKCC1 (Chew et al., 2019), and calpain-mediated proteolysis of the KCC2 CTD is associated with a decrease in transporter activity (Puskarjov et al., 2012). In addition to self-associating, KCCs heterodimerize with other CCCs and interact with other membrane proteins including ion channels (Blaesse et al., 2006; Simard et al., 2007).

Here we report the structure of Mus musculus KCC4 in lipid nanodiscs determined by cryo-EM. The structure reveals unique features of KCCs and, together with functional characterization of structure-based mutants, provides insight into the basis for ion binding, transport, and regulation of KCC4 activity.

2.2 Results

2.2.1 Structure of KCC4 in lipid nanodiscs

Mus musculus KCC4 was heterologously expressed in Spodoptera frugiperda (Sf9) insect cells for purification and structure determination (Figure 2—figure supplement 2). To assess the activity of KCC4 in these cells, we utilized an assay that depends on the ability of KCCs to transport Tl+ in addition to K+(Zhang et al., 2010). In cells loaded with the Tl+-sensitive fluorophore FluxOR red, Tl+ uptake from the extracellular solution results in an increase in fluorescence signal (Figure 1A). Cells infected with virus encoding KCC4, but not cells infected with a virus encoding an anion-selective volume-regulated ion channel SWELL1 (Kern et al., 2019) or uninfected Sf9 cells, displayed increased fluorescence over time consistent with KCC4 activity (Figure 1B, C). No significant difference in activity was observed between N- and C-terminally GFP-tagged mouse KCC4 (Figure 1B, C), in contrast to a previous report for KCC2 (Agez et al., 2017), and C-terminally tagged KCC4 was used for subsequent study.

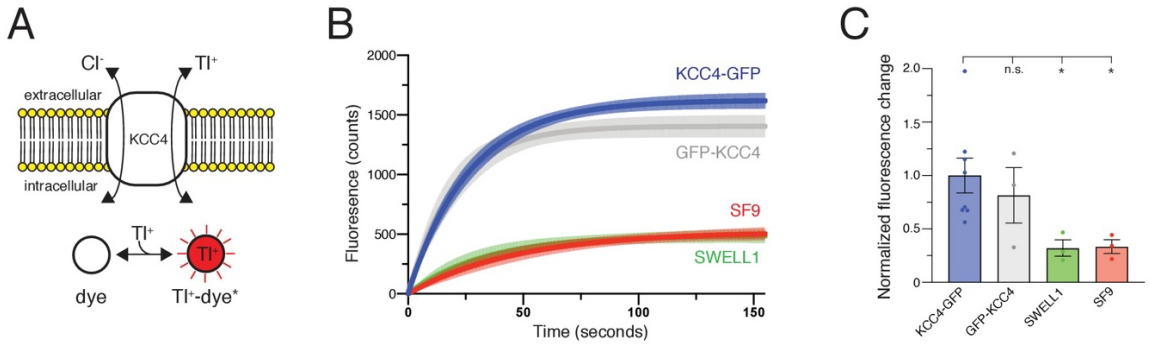

Figure 1: Transport activity of mouse KCC4. (A) Tl^+ uptake assay for KCC4 activity. KCC4 activity in SF9 cells results in Tl^+ uptake and increased fluorescence of the Tl^+ sensitive dye FluxOR Red. (B) Fluorescence values as a function of time for each construct assayed. Lines are global exponential fits to all data with 95% confidence intervals shown for KCC4-GFP (n = 8, blue), GFP-KCC4 (n = 3, gray), SWELL1 (n = 3, green), and uninfected SF9 cells (n = 3 red). (C) Quantification of experiments shown in (B). Normalized final fluorescence. KCC4-GFP 1.0 ± 0.16 (n = 8); GFP-KCC4 0.76 ± 0.33 (n = 3) SWELL1 0.32 ± 0.08 (n = 3) SF9 0.33 ± 0.06 (n = 3); mean ± SEM, one-way Anova (*$p<0.05$, n.s. = not significant).

We reconstituted KCC4 into lipid nanodiscs in order to study the structure of the transporter in a native-like membrane environment. KCC4 was extracted, purified in detergent, and exchanged into nanodiscs formed by the membrane scaffold protein MSP1D1 and a mixture of phospholipids that approximates the composition of major species in neuronal membranes (2:1:1 molar ratio DOPE:POPC:POPS (2-dioleoyl-sn-glycero-3-phosphoethanolamine:1-palmitoyl-2-oleoyl-sn-glycero-3-phosphocholine:1-palmitoyl-2-oleoyl-sn-glycero-3-phospho-L-serine)) (Figure 2—figure supplement 2; Ingólfsson et al., 2017; Ritchie et al., 2009). KCC4-MSP1D1 particles are similar in size and shape to KCC4 particles in detergent micelles by cryo-EM, but show improved distribution in thin ice which enabled reconstruction to high resolution (Figure 2—figure supplement 3).

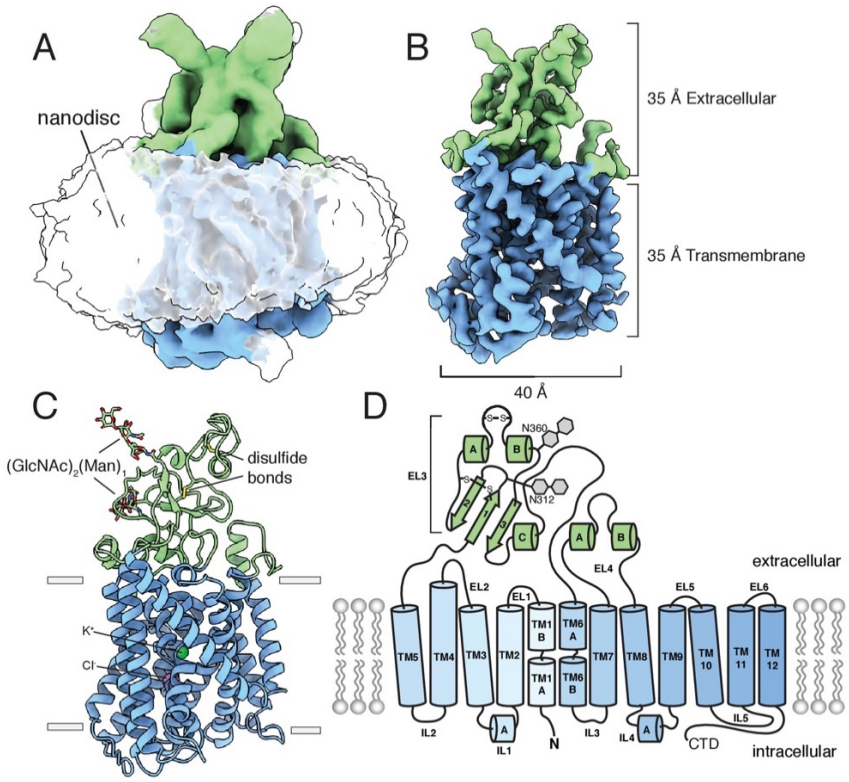

Figure 2: Structure of mouse KCC4 in lipid nanodiscs. (**A**) Cryo-EM map from an unmasked refinement viewed from the membrane plane showing the position of nanodisc, transmembrane region (blue), and extracellular region (green). (**B**) Final map, (**C**) corresponding atomic model, and (**D**) cartoon representation of KCC4. In (**C**), bound K^+ and Cl^- ions are shown as green and violet spheres, respectively. Two disulfides and two N-linked glycosylation sites are shown as sticks and labeled in the cartoon (a third disulfide between TM2 and TM11 is not visible).

An unmasked reconstruction of KCC4 in nanodiscs is shown in Figure 2A contoured to highlight the position of the lipid belt surrounding the transmembrane region. To achieve the highest resolution reconstruction, the nanodisc density was subtracted and particles were subjected to focused classification and subsequent refinement (Figure 2—figure supplement 4). The resulting map, at 3.65 Å overall resolution, enabled complete de novo modeling of the transmembrane and extracellular region of KCC4 and includes two partial extracellular glycosylation sites, a bound K+ ion, and a bound Cl- ion (Figure 2C,D, Figure 2—figure supplements 5 and 6).

2.2.2 Overall architecture

KCC4 is monomeric in the nanodisc structure. Density for the N-terminal region and C-terminal domain (CTD), which together comprise approximately half the expressed protein mass, is not observed in the cryo-EM maps (Figure 2). The N-terminal region is weakly conserved, variable in length among CCCs (Figure 2—figure supplement 1), and is likewise unresolved in the

structures of NKCC1 or KCC1 (Chew et al., 2019; Liu et al., 2019). We presume it is highly flexible in KCC4. The C-terminal domain, while similarly unresolved in KCC1 (Liu et al., 2019), is well conserved, has documented roles in regulation, expression, and trafficking (Arroyo et al., 2013; Marcoux et al., 2017; Payne, 2012; Hartmann and Nothwang, 2014; Rinehart et al., 2009), and mediates homodimerization of NKCC1 and the Archaean CCC (MaCCC) (Chew et al., 2019; Warmuth et al., 2009). We found no evidence of proteolytic cleavage of either region. Mass spectrometry of purified KCC4 showed high coverage (47%) and abundance (81% of all KCC4 peptides) for the CTD (Figure 2—figure supplement 7). We observe a progressive loss of detailed features and decrease in local resolution in TM11 and TM12 that connect the CTD to the core transmembrane region (Figure 2—figure supplements 5B and 6). Some two-dimensional class averages show a blurred cytoplasmic feature in the position we expect the CTD to emerge (Figure 2—figure supplement 3B,D), but attempts to classify distinct conformations of this feature were unsuccessful. We conclude that the monomeric structure reported here corresponds to full-length mouse KCC4 with flexible and/or disordered terminal regions.

The monomeric structure of KCC4 contrasts with recent homodimeric structures of Danio rerio NKCC1 (Chew et al., 2019) and H. sapiens KCC1 (Liu et al., 2019), although dimerization of NKCC1 and KCC1 involve completely distinct interfaces (Figure 3A,C). Disruption of putative tightly associated KCC4 homodimers during purification or sample preparation was excluded for the following reasons: (i) The portion of KCC4 in an early-eluting broad peak from a sizing column (Figure 2—figure supplement 2A) displays nonspecific aggregation by cryo-EM. (ii) KCC4 is monomeric before and after reconstitution in nanodiscs as assessed by cryo-EM (Figure 2—figure supplements 2 and 3). (iii) Cross-linking of purified KCC4 was observed only at high concentrations of crosslinker and was reduced when KCC4 was first deglycosylated (Figure 2—figure supplement 2F), suggesting some cross-linking in glycosylated KCC4 is from intermolecular glycan-glycan or protein-glycan linkages rather than through transmembrane regions or CTDs (Chew et al., 2019). (iv) No substantial differences were observed in the apparent size of KCC4 or KCC1 (assessed by gel filtration) transporters extracted from different expression host cells or treated with different combinations of detergents used in the CCC structure reports to date (Chew et al., 2019; Liu et al., 2019; Figure 2—figure supplement 8).

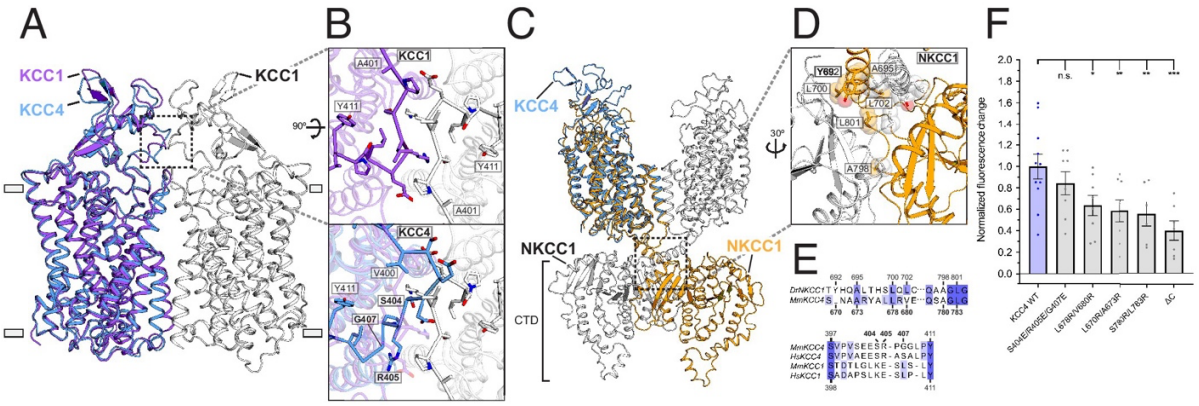

Figure 3: Analysis of putative KCC4 dimerization. (**A**) Overlay of monomeric KCC4 (blue) and dimeric KCC1 (protomer one purple, protomer two white, PDB 6KKT) structures viewed from the membrane. (**B**) Magnified top views of the extracellular protein-protein interaction region of KCC1 (dashed box in (**A**)) shown alone with residues in KCC1 labeled (upper) or with KCC4 overlaid (lower) and KCC4 residues labeled. (**C**) Overlay of KCC4 (blue) and dimeric NKCC1 (protomer one orange, protomer two white, PDB 6NPL) structures viewed from the membrane. (**D**) Magnified view of the intracellular protein-protein interaction region of NKCC1 (dashed box in (**C**)). Residues in NKCC1 for which corresponding KCC4 mutations were made are labeled. (**E**) Partial sequence alignments between KCC4 and NKCC1 (above) and human and mouse KCC1 and KCC4 (below) for the regions highlighted in (**B,D**). Residues mutated in KCC4 are numbered in bold. (**F**) Normalized activity of KCC4 mutations. Wild-type KCC4 1 ± 0.11 (n = 11); S404E, R405E, G407E 0.85 ± 0.11 (n = 8); L678R, V680R 0.59 ± 0.10 (n = 8); L670R, A673R 0.64 ± 0.10 (n = 8); S780R, L783R 0.56 ± 0.11 (n = 6); KCC4ΔC (1–658 0.40 ± 0.09 (n = 7); mean ± SEM, one-way Anova (*p<0.05, **p<0.01 ***p<0.001).

We asked whether there are functional consequences of putative KCC4 dimerization through interfaces similar to those observed in KCC1 or NKCC1 structures. The KCC1 dimeric interface is mediated predominantly through protein-detergent interactions between TM regions and protein-protein interactions between an extracellular loop (Liu et al., 2019; Figure 3A, B). Notably, this loop is poorly conserved in KCCs (Figure 3E). In KCC4, the loop is incompatible with forming a dimer interface without substantial rearrangement due to steric clashes (Figure 3B). A triple mutation designed to disrupt the interaction between extracellular loops in KCC4 (S404E, R405E, G407E) has no effect on transport activity (Figure 3B, F). This mutation (and those described later) did not substantially alter KCC4 folding or expression (Figure 3—figure supplement 1). We conclude dimerization as observed in the KCC1 structure (Liu et al., 2019) is not functionally relevant for KCC4.

In NKCC1, dimerization is mediated predominantly through extensive protein-protein interactions in the CTD (Chew et al., 2019). These regions appear well conserved in KCCs (Figure 3E, Figure 2—figure supplement 1). Three pairs of mutations designed to disrupt CTD-CTD interactions in KCC4 (L678R, V680R; L670R, A673R; and S780R, L783R) resulted in a similar, but incomplete, reduction in KCC4 activity (by an average of 36, 41, and 44%, respectively) (Figure 3C,D,F). This reduction is comparable to that observed in a truncated

KCC4 construct missing the entire C-terminal region (KCC4ΔC, which includes amino acids 1–658) (Figure 3F). These results suggest that monomeric KCC4 is active and that dimerization through the CTDs in a manner analogous to NKCC1 increases transport activity.

2.2.3 Transporter conformation

KCC4 adopts an inward-open conformation. The outer surface of the transporter is sealed from the extracellular solution, while a continuous cavity extends from the center of the transmembrane region to the cytoplasmic side (Figure 4). The transmembrane region consists of twelve helices (TM1-TM12) with TM1-TM5 related to TM6-TM10 through an inverted repeat. TM2 and TM11 in KCC4 are linked by a membrane-buried disulfide bond between amino acids C163 (TM2) and C626 (TM11) conserved between KCCs, but not other CCCs (Figure 2—figure supplement 1).

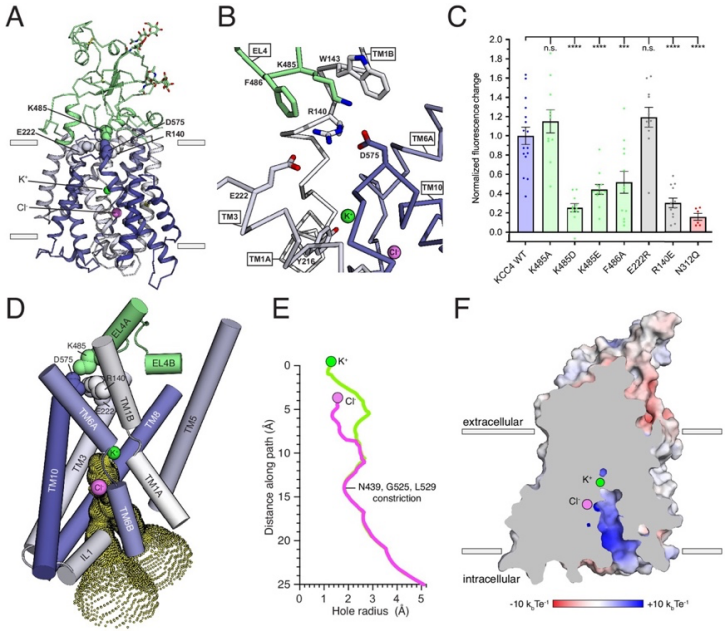

Figure 4: Inward-open conformation of KCC4. (**A**) Cartoon representation of KCC4 colored with extracellular region green and transmembrane region colored in a gradient from white to blue from N- to C-terminus. Ions and residues forming an extracellular gate are shown as spheres. (**B**) Close-up view of extracellular gate. Residues forming the interaction network are shown as sticks. (**C**) Normalized activity of KCC4 mutations. Wild-type KCC4 1 ± 0.09 (n = 16); K485A 1.15 ± 0.12 (n = 11); K485D 0.25 ± 0.04 (n = 11); K485E 0.44 ± 0.05 (n = 12); F486A 0.52 ± 0.11 (n = 12); E222R 1.19 ± 0.10 (n = 11); R140E 0.30 ± 0.05 (n = 12); N312Q 0.16 ± 0.04 (n = 6); mean ± SEM, one-way Anova (***p<0.001, ****p<0.0001). (**D**) View of the open pathway to the intracellular ion binding sites. Helices surrounding the ion binding sites are shown as cylinders. Yellow dots demarcate the surface of a bifurcated tunnel that connects the ion binding sites to the cytoplasmic solution. (**E**) Radius of the ion access tunnel as a function of distance along the path for Cl^- (pink) and K^+ (green). (**F**) Electrostatic surface representation of KCC4 sliced to show one leg of the cytoplasmic access tunnel.

A prominent feature of KCC4 is a large extracellular domain, unique among proteins of known structure, extending ~35 Å above the membrane. It is formed by EL3 (the long extracellular loop; Hartmann et al., 2010) and EL4, which pack together and cover ~2/3 of the transporter outer surface (Figures 2C–D and 4A). Sequence comparison suggests it is conserved in all KCCs and not found in other CCCs (Figure 2—figure supplement 1). The structure consists of a short three-stranded antiparallel beta sheet (EL4 S1-3), five short helices (EL3 HA-C and EL4 HA,B), and regions without regular secondary structure. It is stabilized by two disulfide bonds (C308-C323 and C343-C352) (Hartmann et al., 2010) and decorated with N-linked glycosylation sites (Marcoux et al., 2017; Weng et al., 2013) conserved among KCCs. Non-protein density consistent with glycosylation is present at four previously identified sites (N312, N331, N344, and N360) (Weng et al., 2013) and we model partial carbohydrate chains at the two stronger sites (N312 and N360). Notably, the carbohydrate chain at N312 projects from the EH3 S1-S2 loop underneath an extended segment that leads to TM6A. This arrangement may stabilize the extracellular domain and couple it to movements in TM6A, which moves between functional states in other APC transporters (Shi, 2013; Yamashita et al., 2005; Krishnamurthy and Gouaux, 2012). Indeed, mutation of this site (N312Q) to prevent glycosylation severely reduces KCC4 activity (by an average of 84%, Figure 4C). These results provide a structural explanation for functional defects associated with non-glycosylated mutants of KCC4 (Weng et al., 2013).

The position of the extracellular domain suggests its involvement in conformational changes during the KCC transport cycle. A segment of the extracellular domain close to the membrane forms a constriction that seals the internal vestibule from the extracellular solution. This is likely the extracellular gate based on comparison to other APC transporters (Figure 4A,B; Shi, 2013). In KCC4, residues in EL4, TM1, TM3, and TM10 form an electrostatic and hydrophobic interaction network that seals the gate (Figure 4A, B). R140 on TM1B extends towards the extracellular solution to interact with D575 on TM10 and E222 on TM3. The extracellular domain is positioned immediately above through an interaction between K485 on EL4 and D575. The outer portion of TM1B contributes W143 which, together with F486, surrounds K485 as it projects towards TM10. This is reminiscent of the extracellular gate in LeuT formed by an electrostatic interaction between TM1 and TM10 (R30 and D404) and capped by EL4 through an interaction with TM10 (D401 and A319) (Krishnamurthy and Gouaux, 2012).

We generated mutations at sites in this interaction network to assess its importance for KCC4 function. Disruption of the interaction from the extracellular domain (K485D, K485E, and F486A) or the TM region (R140E) significantly reduced KCC4 transport activity (Figure 4C). The functional effects of these mutations are likely due to specific disruption of the interaction between the TM region and extracellular domain because a more subtle change (K485A) or mutation of a nearby, but less conformationally restricted, residue (E222R) had no effect on activity (Figure 4C). By analogy to LeuT and other APC transporters, these data suggest opening of the KCC4 extracellular gate likely requires ‘unzipping’ of the electrostatic network and

rotation of EL4 and the extracellular domain away from the surface of the TM region (Krishnamurthy and Gouaux, 2012; Penmatsa and Gouaux, 2014).

On the intracellular side of KCC4, a hydrophilic cavity is formed by TM1, TM3, TM6, and TM8 that exposes the inside of the transporter to the cytoplasm (Figure 3C–E). At the top of this cavity are Cl- and K+ binding sites. The cavity forms a bifurcated pathway for ion access to these sites, splitting into two routes approximately halfway through the tunnel due to the position of side chains of N439, R440, and R528. Both sides are open to an essentially equivalent degree (Figure 4D). The only constriction outside of the local area surrounding the ions is formed at the position of N439 (from TM6B), G525, and L529 (from TM8) where the cavity narrows to ~3.6 Å in diameter, still sufficiently large for passage of K+ and Cl- ions. Within ~3 Å of each ion, the cavity narrows such that it would require at least partial ion dehydration.

The cavity surface is markedly electropositive (Figure 4E). From the intracellular solution up to the position of the Cl-, charged and polar side chains (from R440, R528, R535, N131, N274, N439, and N521), backbone amides (from IL1), and a helical dipole (from TM6B) contribute electropositive character. Since intracellular Cl- ions are typically present at lower concentrations than K+ ions, this may serve to favor accumulation of the less abundant substrate near its binding site within transporter. Above the Cl- site and around the K+ site, the accessible surface becomes electronegative and would favor cation binding. The extracellular surface of the transporter outside of the sealed gate is markedly electronegative. How this relates to mechanisms for ion binding and release in outward-open states awaits additional structural information.

2.2.4 Ion binding sites

The central discontinuities in TM1 and TM6 result in protein backbone carbonyls and amides not involved in regular hydrogen bonding that are utilized in other APC transporters for substrate binding (Shi, 2013). Around this region, we observe two prominent non-protein density features (Figure 5A,D). Based on structural, functional, and comparative analyses described below, we model these sites as bound K+ and Cl- ions.

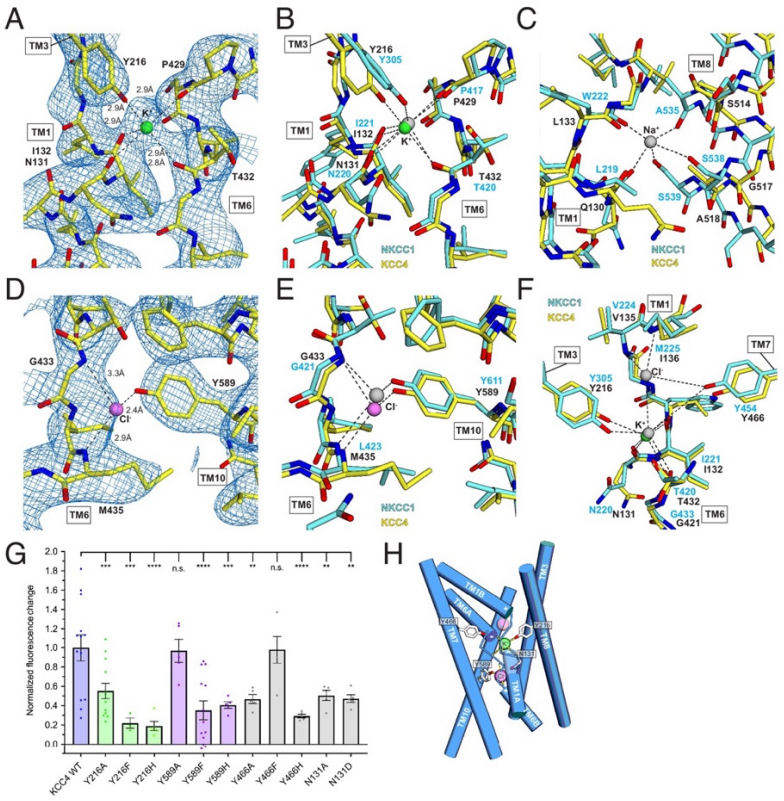

Figure 5: Ion binding sites. (**A**) K^+ binding site. The cryo-EM map is shown as blue mesh and KCC4 is colored with carbon yellow, oxygen red, nitrogen blue, and K^+ green. K^+-coordination environment is indicated with dashed lines. (**B**) Superposition of K^+ binding sites in KCC4 (depicted as in (**A**)) and *Danio rerio* NKCC1 (PDB 6NPL) colored with carbons cyan and K^+ gray. (**C**) Superposition of the Na^+(gray) binding site in NKCC1 and analogous region in KCC4. The position of the Na^+ ion is inferred from SiaT (PDB:5NVA). (**D**) Cl^- (pink) binding site and (**E**) superposition of Cl^- binding site in KCC4 with analogous lower site in NKCC1. (**F**) Superposition of second upper Cl^-binding site in NKCC1 with analogous site in KCC4. (**G**) Normalized activity of KCC4 mutations. Wild-type KCC4 1 ± 0.14 (n = 13); Y216A 0.55 ± 0.08 (n = 13); Y216F 0.22 ± 0.05 (n = 3); Y216H 0.19 ± 0.05 (n = 5); Y589A 0.97 ± 0.12 (n = 5); Y589F 0.35 ± 0.10 (n = 13); Y589H 0.41 ± 0.03 (n = 5); Y466A 0.47 ± 0.05 (n = 5); Y466F 0.98 ± 0.14 (n = 5); Y466H 0.29 ± 0.02 (n = 5); N131A 0.50 ± 0.05 (n = 5); N131D 0.47 ± 0.04 (n = 5); all mean ± SEM, one-way Anova (**p<0.01, ***p<0.001 ****p<0.0001). (**H**) Model for ion binding and transport stoichiometry in CCC transporters. Helices are shown as cylinders with ion coordination in KCC4 shown as dashed lines to green K^+ and pink Cl^-. Helix dipoles in discontinuous helices TM1 and TM6 are indicated. A second upper Cl^- site in NKCC1 and KCC1 not observed in the current KCC4 structure is shown as a transparent pink sphere.

The stronger of the two densities between TM1, TM6, and TM3 is modeled as a K+ ion (Figure 5A). It is surrounded by electronegative groups contributed by backbone carbonyls (N131 and I132 in TM1 and P429 and T432 in TM6) and a tyrosine hydroxyl from Y216 in TM3. The distances between electronegative groups and the ion are consistent with K+ binding (2.8–2.9 Å). The electronegative helix dipoles created by TM1A and TM6A may additionally contribute to a favorable electrostatic environment for cation binding. The coordinating tyrosine is conserved in all CCC family members that transport K+. In NCC, the position corresponding to Y216 is

substituted by a histidine, which likely explains its K+-independence (Figure 2—figure supplement 1).

The second site, between TM6 and TM10, is modeled as a Cl- ion (Figure 5C). It is surrounded by electropositive groups from backbone amides (G433 and I434 in TM6) and a tyrosine hydroxyl from Y589 in TM10. The electropositive helix dipoles created by TM1B and TM6B may additionally stabilize anion binding. The interaction distances and coordination environment are reminiscent of Cl- sites in CLC transporters (Dutzler et al., 2003) and the coordinating tyrosine is conserved across CCCs.

To validate the assignment of the K+ and Cl- sites and test the importance of coordinating residues in transporter activity, we mutated Y216 and Y589 that contribute to the binding sites to A, F, and H and assessed transporter activity. Mutations at both sites resulted in a marked loss in transport activity in the Tl+-flux assay: K+-coordinating Y216 mutations Y216A, Y216F, Y216H and Cl--coordinating Y589 mutations Y589F and Y589H reduced activity (by an average of 45, 78, 81, 65% and 59%, respectively) (Figure 5G). Altering the electrostatic character around the Cl- site with mutations N131A and N131D resulted in comparable transport defects. We conclude the observed K+ and Cl- sites are critical for KCC4 activity.

How does substrate binding in the 1:1 K+:Cl- cotransporter KCC4 differ from the 1:1:2 Na+:K+:Cl- cotransporter NKCC1 (Warmuth et al., 2009; Wahlgren et al., 2018)? The KCC4 K+ and Cl- sites correspond closely to sites for the same ions in NKCC1 (Figure 5B,E). However, the proposed Na+ site in NKCC1 is dramatically reorganized in KCC4 (Figure 5C). In KCC4, TM8 is rotated farther away from TM1 and two consecutive Na+-coordinating serines in NKCC1 (conserved in all Na+-transporting CCCs) are substituted by glycine and alanine in KCC4 (and in KCC1-3) (Figure 2—figure supplement 1). The consequence is a loss of three of the five Na+-coordinating positions, providing a structural explanation for Na+-independence in KCCs.

A second Cl- site in NKCCs extracellular to the K^+ site is structurally conserved in KCC4 (Figure 5F), but we do not observe evidence for ion occupancy at this site in the structure. Interestingly, this site is occupied in a recent structure of KCC1 in addition to the K^+ and Cl^- sites observed in KCC4 (Liu et al., 2019). Mutagenesis of a nearby tyrosine Y466A and Y466H reduce activity of KCC4, suggesting that the integrity of both sites is important for transport (Figure 5G). Understanding how stoichiometric transport of 1 Cl^- with 1 K^+ in KCC4 is accomplished will require structures in additional functional states.

2.3 Discussion

Our structural and mutational data are consistent with prior evidence for monomeric KCCs in cells in addition to homodimers and other heterooligomers (Blaesse et al., 2006; Puskarjov et al., 2012; Watanabe et al., 2009). Comparison of residues in KCC4 that correspond to those in the KCC1 homodimerization interface (Liu et al., 2019) suggest this interaction is not relevant for KCC4 function. However, comparison to the NKCC1 homodimerization interface (Chew et al., 2019) suggest KCC4 could similarly self-interact and mutational data suggests this interaction increases KCC4 activity. A recently posted report of KCC2 and KCC3 structures appears to show a homodimeric interaction through the CTDs very similar to that observed in NKCC1 (Chi, 2020). If monomeric and dimeric KCC4 are functionally distinct, regulated oligomerization in cells would be an opportunity to modulate transport activity. In addition to an increase in basal activity, dimerization involving a close juxtaposition of CTDs and transmembrane regions could enable regulation of transporter activity through CTD posttranslational modifications that may not be possible in monomeric KCC4 with a flexibly attached CTD (Hartmann and Nothwang, 2014; Blaesse et al., 2006; Puskarjov et al., 2012; Watanabe et al., 2009). In support of the in vivo relevance of this regulatory mode, a monomeric to dimeric transition in KCC2 has been correlated with an increase in transporter activity (Blaesse et al., 2006) and is influenced by phosphorylation of the CTD (Watanabe et al., 2009), while proteolytic cleavage of the KCC2 CTD correlates with a decrease in activity (Puskarjov et al., 2012). The ability of KCC4 to hetero-oligomerize with CCCs and other membrane proteins may be associated with weaker self-interaction compared to other CCCs (Simard et al., 2007; Mahadevan et al., 2014; Goutierre et al., 2019; Ivakine et al., 2013).

The structure of KCC4 provides insight into the architecture of KCCs and the mechanistic basis for coupled K^+:Cl^- transport. KCC4 is observed in an inward-open conformation that exposes the inside of the transporter to the cytoplasm through a wide and electropositive tunnel that may serve to concentrate the less abundant intracellular substrate Cl^-. This conformation is similar to that observed in NKCC1 and KCC1 and presumably represents the lowest energy state for CCCs in symmetrical salt concentrations and the absence of a transmembrane electrical gradient (Chew et al., 2019; Chi, 2020). We identify K+ and Cl- ions around central discontinuities in TM1 and TM6. A Na+ site in the 1:1:2 Na^+:K^+:Cl^- cotransporter NKCC1 is reorganized in KCC4 due to TM-TM displacement and loss of specific coordinating side chains, explaining Na+-independence in KCCs.

2.4 Materials and Methods

2.4.1 Cloning and protein expression

Cloning, expression, and purification were performed similarly to that described for LRRC8A (Kern et al., 2019). The sequence for KCC4 and KCC1 from Mus musculus were codon optimized for Spodoptera frugiperda and synthesized (Thermo Fisher, Cambridge, MA).

Sequences were cloned into a custom vector based on the pACEBAC1 backbone (MultiBac; Geneva Biotech, Geneva, Switzerland) with an added C-terminal PreScission protease (PPX) cleavage site, linker sequence, superfolder GFP (sfGFP), and 7xHis tag, generating a construct for expression of mmKCC4-SNS-LEVLFQGP-SRGGSGAAAGSGSGS-sfGFP-GSS-7xHis. Mutations were introduced using standard PCR techniques with partially overlapping primers. MultiBac cells were used to generate bacmids according to manufacturer's instructions. Spodoptera frugiperda (Sf9) cells were cultured in ESF 921 medium (Expression Systems, Davis, CA) and P1 virus was generated from cells transfected with Escort IV Transfection Reagent (Sigma, Carlsbad, CA) according to manufacturer's instructions. P2 virus was generated by infecting cells at 2 × 106 cells/mL with P1 virus at a MOI ~ 0.1. Infection monitored by fluorescence of sfGFP-tagged protein and P2 virus was harvested at 72 hr post infection. P3 virus was generated in a similar manner to expand the viral stock. The P3 viral stock was then used to infect 1 L of Sf9 cells at 4 × 106cells/mL at a MOI ~ 2–5. At 60 hr post-infection, cells were harvested by centrifugation at 2500 x g and frozen at −80°C.

2.4.2 Transporter assay

The FluxOR-Red Potassium Ion Channel Assay (Thermo Fisher Scientific) was adapted for transport assays in Sf9 insect cells by adjusting the osmolarity of all buffers to 380 mOsm (by addition of sodium methylsulfonate). Cells were infected at a density of 1.5 × 106 cells/ml and grown in suspension for 60–72 hr for robust KCC4-GFP expression. 100 uL of cells at 1 × 106 cells/ml were plated and allowed to adhere for 1 hr before the assay. For experiments in Figures 3–5, 100 uL of cells at 1 × 106 cells/ml were plated and allowed to adhere for 1 hr before viral infection. Cells were grown for 60–72 hr for robust transporter expression prior to assay. Growth media was replaced with 1X Loading Buffer and incubated at 27°C away from light for 1 hr. The FluxOR Red reagent is a non-fluorescent indicator dye which is loaded into cells as a membrane-permeable acetoxymethyl (AM)-ester. The non-fluorescent AM ester of the FluxOR Red reagent is cleaved by endogenous esterases into a fluorogenic Tl^+-sensitive indicator. 1X Loading Buffer was subsequently removed and replaced with Dye-free Assay Buffer and FluxOR Background Suppressor. The assay was performed in 96-well, black-walled, clear-bottom plates (Costar). For data in Figure 1, fluorescence was measured on a Perkin-Elmer Envision Multilabel Plate Reader using bottom read fluorescence and a BODIPY TMR FP filter set (excitation 531 nm and 25 nm bandwidth, emission 595 nm and 60 nm bandwidth). For data in Figures 3–5, Fluorescence was measured on a Molecular Devices SpectraMax M3 using bottom read fluorescence and an excitation 560 nm with auto cutoff at 590 nm and emission 590 nm. The recordings were baseline corrected by subtracting the average fluorescence from 180 s prior to the addition of Basal Potassium Stimulus buffer and time zero is defined as the first data point recorded after the addition of stimulus. Global fits of all data to a one phase association model Y=(Plateau)*(1-e(-x/τ)) are displayed with 95% confidence interval bands (Figure 1B). Alternatively, the final 50 counts were averaged as a measure of final fluorescence increase and normalized to wild-type

KCC4 fluorescence increase from experiments performed on the same day. In some experiments, average GFP fluorescence was measured between FluxOR fluorescence measurements and used to normalize FluxOR fluorescence values to account for differences in expression level. This normalization did not change results in a significant way and so was not performed for the final data presented.

2.4.3 Protein purification

Cells from 1 L of culture (~7–12.5 mL of cell pellet) were thawed in 100 mL of Lysis Buffer (50 mM Tris, 150 mM KCl, 1 mM EDTA, pH 8.0). Protease inhibitors were added to the lysis buffer immediately before use (final concentrations: E64 (1 µM), Pepstatin A (1 µg/mL), Soy Trypsin Inhibitor (10 µg/mL), Benzimidine (1 mM), Aprotinin (1 µg/mL), Leupeptin (1 µg/mL), and PMSF (1 mM)). Benzonase (5 µl) was added after cells thawed. Cells were then lysed by sonication and centrifuged at 150,000 x g for 45 min. The supernatant was discarded, and residual nucleic acid was removed from the top of the membrane pellet by rinsing with DPBS. A 10%/2% and 10%/1% w/v solution of DDM/CHS was clarified by bath sonication in 200 mM Tris pH 8.0 and subsequently added to buffers at the indicated final concentrations. Membrane pellets were transferred to a glass dounce homogenizer containing Extraction Buffer (50 mM Tris, 150 mM KCl, 1 mM EDTA, 1% w/v n-Dodecyl-β-D-Maltopyranoside (DDM, Anatrace, Maumee, OH), 0.2% w/v Cholesterol Hemisuccinate Tris Salt (CHS, Anatrace), pH 8.0). Membrane pellets were homogenized in Extraction Buffer and this mixture (100 mL final volume) was gently stirred at 4°C for 1 hr. The extraction mixture was centrifuged at 33,000 x g for 45 min. The supernatant, containing solubilized KCC4-sfGFP, was bound to 5 mL of Sepharose resin coupled to anti-GFP nanobody for 1 hr at 4°C. The resin was collected in a column and washed with 20 mL of Buffer 1 (20 mM Tris, 150 mM KCl, 1 mM EDTA, 0.025% DDM, 0.005% CHS, pH 8.0), 50 mL of Buffer 2 (20 mM Tris, 500 mM KCl, 1 mM EDTA, 0.025% DDM, 0.005% CHS, pH 8.0), and 20 mL of Buffer 1. Washed resin was resuspended in 6 mL of Buffer 1 with 0.5 mg of PPX and rocked gently in the capped column overnight. Cleaved KCC4 protein was eluted with an additional 25 mL of Buffer 1. The eluted pool was concentrated to ~500 µl with an Amicon Ultra spin concentrator 100 kDa cutoff (MilliporeSigma, USA) and subjected to size exclusion chromatography using a Superose 6 Increase column (GE Healthcare, Chicago, IL) run in Buffer 3 (20 mM Tris pH 8.0, 150 mM KCl, 1 mM EDTA, 0.025% DDM, 0.0025% CHS) on a NGC system (Bio-Rad, Hercules, CA). Peak fractions containing KCC4 transporter were collected and concentrated.

2.4.4 Fluorescence size exclusion chromatography (FSEC)

Sf9 cells were plated at 1 × 106 cells/ml into six well plates and allowed to adhere for 1 hr prior to viral infection at a ratio of 1:30 (v/v). Cells were harvested after 60–72 hr, pelleted by centrifugation, and frozen. Transfected HEK 293T GNTI- cells were prepared using

Lipofectamine 2000 according to manufacturer's instructions. Media was switched 18 hr post-transfection to fresh media with 10 mM sodium butyrate. Cells were incubated for 19 hr longer at 30°C, harvested, pelleted by centrifugation, and frozen.

Frozen samples containing ~8 million infected Sf9 cells and ~1 million transfected HEK 293T GNTI- cells were thawed, extracted for 1 hr at 4°C, and pelleted at 21,000 x g at 4°C for 1 hr. Supernatant was run on a Superose 6 Increase column with fluorescence detection for GFP. For mutant comparisons (Figure 3—figure supplement 1), extraction buffer was (50 mM Tris pH 8, 150 mM KCl, 1 mM EDTA, all protease inhibitors used for protein purification, 1% DDM, 0.2% CHS) and running buffer was (20 mM Tris pH8, 150 mM KCl, 1 mM EDTA, 0.025% DDM, 0.0025% CHS). The same buffers were used for the 'DDM/CHS' conditions in Figure 2—figure supplement 8A,B,C and in Figure 2—figure supplement 8D,E except that running buffer in Figure 2—figure supplement 8E contained (0.025% DDM, 0.005% CHS). The 'GDN' condition used in Figure 2—figure supplement 8A,B,C corresponds to conditions used for KCC1 structure determination (Liu et al., 2019). Extraction buffer was (20 mM Tris pH8, 150 mM KCl, all protease inhibitors used for protein purification, 2% DDM, 0.2% CHS). Running buffer was (20 mM Tris pH8, 150 mM KCl, 0.06% GDN). The 'Digitonin' condition used in Figure 2—figure supplement 8A,B,C corresponds to conditions used for NKCC1 structure determination (Chew et al., 2019). Extraction buffer was (50 mM Tris pH 8, 150 mM KCl, 1 mM EDTA, all protease inhibitors used for protein purification, 1% LMNG, 0.01% CHS) and running buffer was (20 mM Tris pH8, 150 mM KCl, 1 mM EDTA, 0.06% Digitonin).

2.4.5 Cross-linking and mass spectrometry

Fractions corresponding to peaks 1 and 2 from size exclusion chromatography were separately pooled and concentrated to 0.5 mg/mL. Crosslinking was performed by adding 1 uL of glutaraldehyde from 10X stock solutions in water to 10 uL of KCC4 to achieve final glutaraldehyde concentrations of 0.02, 0.01, 0.005, 0.0025, and 0%. Samples were incubated for 30 min prior to quenching by addition of 1 uL 1M Tris-HCl and analysis by SDS-PAGE on 4–12% Tris-glycine gel (BioRad, USA). Deglycosylated samples were pretreated with 1:10 vol purified PNGase at 1 mg/mL (Addgene 114274) for 1 hr at 4°C prior to the addition of glutaraldehyde.

For mass spectrometry, the band corresponding to purified KCC4 was excised from a 4–12% Tris-glycine gel, digested with trypsin in situ, and the resulting peptides extracted and concentrated. Mass spectrometry was performed by the Vincent J. Coates Proteomics/Mass Spectrometry Laboratory at UC Berkeley. A nano LC column was packed in a 100 μm inner diameter glass capillary with an emitter tip. The column consisted of 10 cm of Polaris c18 5 μm packing material (Varian), followed by 4 cm of Partisphere 5 SCX (Whatman). The column was loaded by use of a pressure bomb and washed extensively with buffer A (5% acetonitrile/0.02%

heptaflurobutyric acid (HBFA)). The column was then directly coupled to an electrospray ionization source mounted on a Thermo-Fisher LTQ XL linear ion trap mass spectrometer. An Agilent 1200 HPLC equipped with a split line so as to deliver a flow rate of 300 nl/min was used for chromatography. Peptides were eluted using a 4-step MudPIT procedure (Washburn et al., 2001). Buffer A was 5% acetonitrile/0.02% heptaflurobutyric acid (HBFA); buffer B was 80% acetonitrile/0.02% HBFA. Buffer C was 250 mM ammonium acetate/5% acetonitrile/0.02% HBFA; buffer D was same as buffer C, but with 500 mM ammonium acetate.

Protein identification was done with Integrated Proteomics Pipeline (IP2, Integrated Proteomics Applications, Inc San Diego, CA) using ProLuCID/Sequest, DTASelect2 and Census (Xu et al., 2015; Tabb et al., 2002; Park et al., 2008). Tandem mass spectra were extracted into ms1 and ms2 files from raw files using RawExtractor (McDonald et al., 2004). Data was searched against a Spodoptera frugiperda protein database with the purified mouse KCC4 sequence added, supplemented with sequences of common contaminants, and concatenated to form a decoy database (Peng et al., 2003). LTQ data was searched with 3000.0 milli-amu precursor tolerance and the fragment ions were restricted to a 600.0 ppm tolerance. All searches were parallelized and searched on the VJC proteomics cluster. Search space included all half tryptic peptide candidates with no missed cleavage restrictions. Carbamidomethylation (+57.02146) of cysteine was considered a static modification. In order to identify authentic termini, we required one tryptic terminus for each peptide identification. The ProLuCID search results were assembled and filtered using the DTASelect program with a peptide false discovery rate (FDR) of 0.001 for single peptides and a peptide FDR of 0.005 for additional peptides for the same protein. Under such filtering conditions, the estimated false discovery rate was less than 1%.

2.4.6 Nanodisc reconstitution

Freshly purified and concentrated KCC4 in Buffer three was reconstituted into MSP1D1 nanodiscs with a mixture of lipids (DOPE:POPS:POPC at 2:1:1 molar ratio, Avanti, Alabaster, Alabama) at a final molar ratio of KCC4:MSP1D1:lipids of 0.2:1:50. Lipids in chloroform were prepared by mixing, drying under argon, washing with pentane, drying under argon, and placing under vacuum overnight. The dried lipid mixture was rehydrated in Buffer 4 (20 mM Tris, 150 mM KCl, 1 mM EDTA pH 8.0) and clarified by bath sonication. DDM was added to a final concentration of 8 mM and the detergent solubilized lipids were sonicated until clear. Lipids, Buffer 4 containing 8 mM DDM, and KCC4 protein were mixed and incubated at 4°C for 30 min before addition of purified MSP1D1. After addition of MSP1D1, the nanodisc formation solution was 47.5 µM KCC4, 104 µM MSP1D1, 13 mM DOPE:POPS:POPC, and 4 mM DDM in Buffer 4 (final concentrations). After mixing at 4°C for 30 mins, 60 mg of Biobeads SM2 (Bio-Rad, USA) (prepared by sequential washing in methanol, water, and Buffer four and weighed damp following bulk liquid removal) were added and the mixture was rotated at 4°C overnight (~12 hr). Nanodisc-containing supernatant was collected and spun for 10 min at 21,000 x g before

loading onto a Superose 6 Increase column in Buffer 4. Peak fractions corresponding to KCC4-MSP1D1 were collected and spin concentrated using a 100 kDa cutoff for grid preparation.

2.4.7 Grid preparation

The KCC4-MSP1D1 nanodisc sample was concentrated to ~1 mg/mL and centrifuged at 21,000 x g for 10 min at 4°C prior to grid preparation. A 3 uL drop of protein was applied to a freshly glow discharged Holey Carbon, 400 mesh R 1.2/1.3 gold grid (Quantifoil, Großlöbichau, Germany). A Vitrobot Mark IV (FEI/Thermo Scientific, USA) was utilized for plunge freezing in liquid ethane with the following settings: 4°C, 100% humidity, one blot force, 3 s blot time, 5 s wait time. The KCC4 detergent sample was frozen at 4.5 mg/mL and centrifuged at 21,000 x g for 10 min at 4°C prior to grid preparation. A 3 µL drop of protein was applied to a freshly glow discharged Holey Carbon, 400 mesh R 1.2/1.3 gold grid. A Vitrobot Mark IV (FEI/Thermo Scientific, USA) was utilized for plunge freezing in liquid ethane with the following settings: 4°C, 100% humidity, one blot force, 4 s blot time, 1 s wait time. Grids were clipped in autoloader cartridges for data collection.

2.4.8 Data collection

KCC4-MSP1D1 grids were transferred to a Talos Arctica cryo-electron microscope (FEI/Thermo Scientific, USA) operated at an acceleration voltage of 200 kV. Images were recorded in an automated fashion with SerialEM (Mastronarde, 2005) using image shift with a target defocus range of −0.7 ~ −2.2 µm over 5 s as 50 subframes with a K3 direct electron detector (Gatan, USA) in super-resolution mode with a super-resolution pixel size of 0.5685 Å. The electron dose was 9.333 e- / Å (Marcoux et al., 2017)/s (0.9333 e-/ Å2/frame) at the detector level and total accumulated dose was 46.665 e-/Å2. KCC4-detergent grids were transferred to a Titan Krios cryo-electron microscope (FEI/Thermo Scientific, USA) operated at an acceleration voltage of 300 kV. Images were recorded in an automated fashion with SerialEM (Mastronarde, 2005) with a target defocus range of −0.7 to −2.2 µm over 9.6 s as 48 subframes with a K2 direct electron detector (Gatan, USA) in super-resolution mode with a super-resolution pixel size of 0.5746 Å. The electron dose was 6.092 e- / Å (Marcoux et al., 2017)/s (1.2184 e- / Å (Marcoux et al., 2017)/frame) at the detector level and total accumulated dose was 58.4832 e-/Å (Marcoux et al., 2017). See also Table 1 for data collection statistics.

2.4.9 Data processing

The processing pipeline is shown in Figure 2—figure supplement 4A–C. We used Cryosparc2 (Punjani et al., 2017) for initial model generation and refinement until reconstructions reached 4–5 Å resolution. Bayesian polishing and nanodisc subtraction in Relion 3.0.7 (Zivanov et al., 2019; Zivanov et al., 2018) were used to achieve highest resolution reconstructions. While the

contribution of disordered or flexible N- and C-terminal regions to alignments is unknown, the remaining 55 kDa asymmetric membrane protein is among the smallest in terms of resolved mass resolved by cryo-EM to date.

A total of 1572 movie stacks were collected, motion-corrected and binned to 1.137 Å/pixel using MotionCor2 (Zheng et al., 2017), and CTF-corrected using Ctffind 4.1.13 (Rohou and Grigorieff, 2015; Figure 2—figure supplement 4A). Micrographs with a Ctffind reported resolution estimate worse than 5 Å were discarded. A small number of particles (~1000) were picked manually and subjected to two-dimensional classification to generate references for autopicking in Relion. 1,826,000 particles were autopicked and extracted at 2.274 Å/pixel (2x binned) for initial cleanup. Non-particle picks and apparent junk particles were removed by several rounds of two-dimensional class averaging. The remaining 887,132 particles were extracted at 1.137 Å/pixel and imported into Cryosparc. An additional round of 2D classification generated a particle set of 491,111. These particles were the input of an ab initio reconstruction (non-default values: four classes, 0.1 class similarity, 4 Å max resolution, per-image optimal scales). 2D classification of particles (160,868) that contributed to the most featured volume resulted in a set of 125,593 particles which were the input of an ab initio reconstruction. Alignments were iteratively improved using non-uniform (NU) refinement (0.89 window inner radius, 120 voxel box size, 10 extra final passes, 10 Å low-pass filter, 0.01 batch epsilon, minimize over per-particle scale, 1–4 Å dynamic mask near, 3–8 Å dynamic mask far, 6–10 Å dynamic mask start resolution, 4–6 Å local processing start resolution). Two separate NU refinement output volumes were input into a heterogeneous refinement job of the 886,528 particle set (forced hard classification, 10 Å initial resolution, five final full iterations). The more featured class (538,280 particles) was heterogeneously refined (forced hard classification, 10 Å initial resolution, five final full iterations) (Figure 2—figure supplement 4B). The particles and volume from one output (354,234 particles) were input into the first of three iterative NU refinements (10 extra final passes for the second and third iteration).

Particle positions and angles from the final cryoSPARC2 refinement job were input into Relion (using csparc2relion.py from the UCSF PyEM [Asarnow, 2016]) and 3D refined to generate a 4.18 Å map (6 Å low-pass filter, 0.9 degrees initial sampling, 0.9 degrees local searches) (Figure 2—figure supplement 4C). A second 3D refinement following Bayesian particle polishing improved the map and reported resolution (4.01 Å) (6 Å low-pass filter, 0.9 degrees initial sampling, 0.9 degrees local searches). CTF refinement with beam tilt group estimation and per-particle defocus was performed, although subsequent 3D refinement did not markedly improve the map. Particle subtraction was performed to remove the contribution of the nanodisc density from alignments and subsequent 3D refinement markedly improved the map (reported resolution 3.86 Å or 3.72 Å after postprocessing) (6 Å low-pass filter, 0.9 degrees initial sampling, 0.9 degrees local searches). A final improvement in map quality and reported resolution and was obtained by removing poor particles with a 3D classification job (two classes, 10 Å initial low-

pass filter, 16 tau fudge, no angular sampling). The final particle set (110,143) was subjected to 3D refinement to generate a final map at 3.72 Å resolution (3.65 Å after postprocessing) (6 Å low-pass filter, 0.9 degrees initial sampling, 0.9 degrees local searches). Particle distribution and local resolution was calculated using Relion (Figure 2—figure supplement 5A,B). FSCs reported in Figure 2—figure supplement 5 were calculated using Phenix.mtriage.

2.4.10 Modeling, refinement, and structure analysis

The final cryo-EM maps were sharpened using Phenix.autosharpen (Adams et al., 2010). The structure was modeled de novo in Coot and refined in real space using Phenix.real_space_refine with Ramachandran and NCS restraints. Validation tools in Phenix, EMRinger (Barad et al., 2015), and Molprobity (Chen et al., 2010) were used to guide iterative rounds of model adjustment in Coot and refinement in Phenix. Cavity measurements were made with HOLE implemented in Coot (Emsley et al., 2010). Electrostatic potential was calculated using APBS-PDB2PQR (Dolinsky et al., 2004) Pymol plugin. Figures were prepared using PyMOL, Chimera, ChimeraX, Fiji, Prism, Adobe Photoshop, and Adobe Illustrator software.

2.5 Data availability

The final map of KCC4 in MSP1D1 nanodiscs has been deposited to the Electron Microscopy Data Bank under accession code EMD-20807. Atomic coordinates have been deposited in the PDB under ID 6UKN. Original KCC4 in MSP1D1 nanodiscs micrograph movies have been deposited to EMPIAR under deposition EMPIAR-10394.
The following data sets were generated

1. Reid MS, Kern DM, Brohawn SG (2020) Electron Microscopy Public Image Archive ID 10394. Cryo-EM structure of the potassium-chloride cotransporter KCC4 in lipid nanodiscs. https://www.ebi.ac.uk/pdbe/emdb/empiar/entry/10394
2. Reid MS, Kern DM, Brohawn SG (2019) Electron Microscopy Data Bank ID EMD-20807. Cryo-EM structure of the potassium-chloride cotransporter KCC4 in lipid nanodiscs. http://www.ebi.ac.uk/pdbe/entry/emdb/EMD-20807
3. Reid MS, Kern DM, Brohawn SG (2019) RCSB Protein Data Bank ID 6UKN. Cryo-EM structure of the potassium-chloride cotransporter KCC4 in lipid nanodiscs. http://www.rcsb.org/structure/6UKN

2.6 Acknowledgments

We thank members of the Brohawn and Eunyong Park laboratories for feedback and critical reading of the manuscript. We thank Dr. Dan Toso, Dr. Jonathon Remis, and Paul Tobias at the Berkeley Bay Area Cryo-EM facility and UC Berkeley Talos Arctica facility for assistance with microscope setup and data collection. We thank Dr. Lori Kohlstaedt for assistance with mass

spectrometry. This work used the Vincent J Proteomics/Mass Spectrometry Laboratory at UC Berkeley, supported in part by NIH S10 Instrumentation Grant S10RR025622. We thank Dr. Mary West and Dr. Pingping He of the High-Throughput Screening Facility (HTSF) at UC Berkeley. This work was performed in part in the HTSF, which provided the Perkin-Elmer Envision Multilabel Plate Reader. SGB is a New York Stem Cell Foundation-Robertson Neuroscience Investigator. This work is supported by a UC Berkeley Chancellor's Fellowship (MSR), and a NIGMS postdoctoral fellowship F32GM128263 (DMK), the New York Stem Cell Foundation (SGB), a NIGMS grant DP2GM123496-01 (SGB), a McKnight Foundation Scholar Award (SGB), and a Klingenstein-Simons Foundation Fellowship Award (SGB).

2.7 References

1. Adams PD, Afonine PV, Bunko´ czi G, Chen VB, Davis IW, Echols N, Headd JJ, Hung LW, Kapral GJ, Grosse-Kunstleve RW, McCoy AJ, Moriarty NW, Oeffner R, Read RJ, Richardson DC, Richardson JS, Terwilliger TC, Zwart PH. 2010. PHENIX: a comprehensive Python-based system for macromolecular structure solution. Acta Crystallographica Section D Biological Crystallography 66:213–221.
2. Agez M, Schultz P, Medina I, Baker DJ, Burnham MP, Cardarelli RA, Conway LC, Garnier K, Geschwindner S, Gunnarsson A, McCall EJ, Frechard A, Audebert S, Deeb TZ, Moss SJ, Brandon NJ, Wang Q, Dekker N, Jawhari A. 2017. Molecular architecture of potassium chloride co-transporter KCC2. Scientific Reports 7:14. DOI: https://doi.org/10.1038/s41598-017-15739-1, PMID: 29184062
3. Arroyo JP, Kahle KT, Gamba G. 2013. The SLC12 family of electroneutral cation-coupled chloride cotransporters. Molecular Aspects of Medicine 34:288–298. DOI: https://doi.org/10.1016/j.mam.2012.05.002, PMID: 23506871
4. Asarnow D. 2016. UCSF Pyem. GitHub. https://github.com/asarnow/pyem
5. Barad BA, Echols N, Wang RY, Cheng Y, DiMaio F, Adams PD, Fraser JS. 2015. EMRinger: side chain-directed model and map validation for 3D cryo-electron microscopy. Nature Methods 12:943–946.
6. Bergeron MJ, Gagnon E, Wallendorff B, Lapointe JY, Isenring P. 2003. Ammonium transport and pH regulation by K(+)-Cl(-) cotransporters. American Journal of Physiology. Renal Physiology 285:F68–F78.
7. Bergeron MJ, Frenette-Cotton R, Carpentier GA, Simard MG, Caron L, Isenring P. 2009. Phosphoregulation of K(+)-Cl(-) cotransporter 4 during changes in intracellular cl(-) and cell volume. Journal of Cellular Physiology 219:787–796.
8. Blaesse P, Guillemin I, Schindler J, Schweizer M, Delpire E, Khiroug L, Friauf E, Nothwang HG. 2006. Oligomerization of KCC2 correlates with development of inhibitory neurotransmission. Journal of Neuroscience 26:10407–10419.
9. Boettger T, Hübner CA, Maier H, Rust MB, Beck FX, Jentsch TJ. 2002. Deafness and renal tubular acidosis in mice lacking the K-Cl co-transporter Kcc4. Nature 416:874–878.

10. Chen VB, Arendall WB, Headd JJ, Keedy DA, Immormino RM, Kapral GJ, Murray LW, Richardson JS, Richardson DC. 2010. MolProbity: all-atom structure validation for macromolecular crystallography. Acta Crystallographica Section D Biological Crystallography 66:12–21.
11. Chew TA, Orlando BJ, Zhang J, Latorraca NR, Wang A, Hollingsworth SA, Chen DH, Dror RO, Liao M, Feng L. 2019. Structure and mechanism of the cation-chloride cotransporter NKCC1. Nature 572:488–492.
12. Chi X. 2020. Molecular basis for regulation of human potassium chloride cotransporters. bioRxiv. DOI: https://doi.org/10.1101/2020.02.22.960815
13. Dolinsky TJ, Nielsen JE, McCammon JA, Baker NA. 2004. PDB2PQR: an automated pipeline for the setup of Poisson-Boltzmann electrostatics calculations. Nucleic Acids Research 32:W665–W667.
14. Dunham PB, Stewart GW, Ellory JC. 1980. Chloride-activated passive potassium transport in human erythrocytes.
15. Dutzler R, Campbell EB, MacKinnon R. 2003. Gating the selectivity filter in ClC chloride channels. Science 300:108–112. DOI: https://doi.org/10.1126/science.1082708, PMID: 12649487
16. Emsley P, Lohkamp B, Scott WG, Cowtan K. 2010. Features and development of coot. Acta Crystallographica. Section D, Biological Crystallography 66:486–501.
17. Frenette-Cotton R, Marcoux A-A, Garneau AP, Noel M, Isenring P. 2017. Phosphoregulation of K +-Cl cotransporters during cell swelling: novel insights. Journal of Cellular Physiology 233:396–408.
18. Gamba G. 2005. Molecular physiology and pathophysiology of electroneutral cation-chloride cotransporters.Physiological Reviews 85:423–493. DOI: https://doi.org/10.1152/physrev.00011.2004, PMID: 15788703
19. Goutierre M, Al Awabdh S, Donneger F, Franc¸ ois E, Gomez-Dominguez D, Irinopoulou T, Menendez de la Prida L, Poncer JC. 2019. KCC2 regulates neuronal excitability and hippocampal activity via interaction with Task-3 channels. Cell Reports 28:91–103. DOI: https://doi.org/10.1016/j.celrep.2019.06.001, PMID: 31269453
20. Hartmann AM, Wenz M, Mercado A, Sto¨ rger C, Mount DB, Friauf E, Nothwang HG. 2010. Differences in the large extracellular loop between the K(+)-Cl(-) cotransporters KCC2 and KCC4. The Journal of Biological Chemistry 285:23994–24002. DOI: https://doi.org/10.1074/jbc.M110.144063, PMID: 20516068
21. Hartmann AM, Nothwang HG. 2014. Molecular and evolutionary insights into the structural organization of cation chloride cotransporters. Frontiers in Cellular Neuroscience 8:470. DOI: https://doi.org/10.3389/fncel. 2014.00470, PMID: 25653592
22. Ingo´ lfsson HI, Carpenter TS, Bhatia H, Bremer PT, Marrink SJ, Lightstone FC. 2017. Computational lipidomics of the neuronal plasma membrane. Biophysical Journal 113:2271–2280. DOI: https://doi.org/10.1016/j.bpj.2017. 10.017, PMID: 29113676

23. Ivakine EA, Acton BA, Mahadevan V, Ormond J, Tang M, Pressey JC, Huang MY, Ng D, Delpire E, Salter MW, Woodin MA, McInnes RR. 2013. Neto2 is a KCC2 interacting protein required for neuronal cl- regulation in hippocampal neurons. PNAS 110:3561–3566. DOI: https://doi.org/10.1073/pnas.1212907110, PMID: 23401525
24. Jin SC, Furey CG, Zeng X, Allocco A, Nelson-Williams C, Dong W, Karimy JK, Wang K, Ma S, Delpire E, Kahle KT. 2019. SLC12A ion transporter mutations in sporadic and familial human congenital hydrocephalus. Molecular Genetics & Genomic Medicine 7:e892. DOI: https://doi.org/10.1002/mgg3.892, PMID: 31393094
25. Kahle KT, Khanna AR, Alper SL, Adragna NC, Lauf PK, Sun D, Delpire E. 2015. K-Cl cotransporters, cell volume homeostasis, and neurological disease. Trends in Molecular Medicine 21:513–523. DOI: https://doi.org/10.1016/j.molmed.2015.05.008, PMID: 26142773
26. Karadsheh MF, Byun N, Mount DB, Delpire E. 2004. Localization of the KCC4 potassium-chloride cotransporter in the nervous system. Neuroscience 123:381–391. DOI: https://doi.org/10.1016/j.neuroscience.2003.10.004, PMID: 14698746
27. Kern DM, Oh S, Hite RK, Brohawn SG. 2019. Cryo-EM structures of the DCPIB-inhibited volume-regulated anion channel LRRC8A in lipid nanodiscs. eLife 8:e42636. DOI: https://doi.org/10.7554/eLife.42636, PMID: 30775971
28. Krishnamurthy H, Gouaux E. 2012. X-ray structures of LeuT in substrate-free outward-open and apo inward-open states. Nature 481:469–474. DOI: https://doi.org/10.1038/nature10737, PMID: 22230955
29. Lauf PK, Theg BE. 1980. A chloride dependent K+ flux induced by N-ethylmaleimide in genetically low K+ sheep and goat erythrocytes. Biochemical and Biophysical Research Communications 92:1422–1428. DOI: https://doi.org/10.1016/0006-291X(80)90445-3
30. Liu S, Chang S, Han B, Xu L, Zhang M, Zhao C, Yang W, Wang F, Li J, Delpire E, Ye S, Bai XC, Guo J. 2019. Cryo-EM structures of the human cation-chloride cotransporter KCC1. Science 366:505–508. DOI: https://doi.org/10.1126/science.aay3129, PMID: 31649201

2.8 Supplemental figures

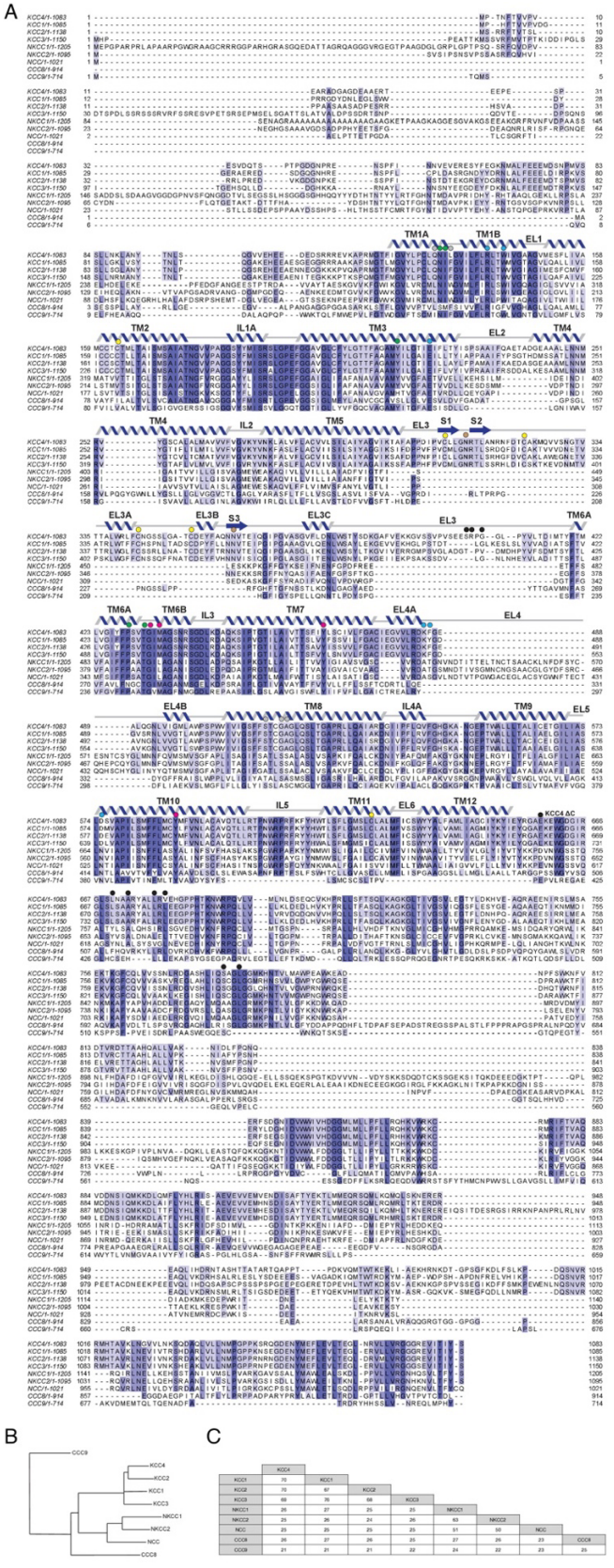

Figure 2 supplement 1: CCC family sequence alignment.
(A) Sequence alignment of mouse CCC family transporters. Sequence numbering is indicated at the left and right of each line. Secondary structure for KCC4 is indicated above the sequence. Residues discussed in the text are indicated with circles above the sequence: green, K^+ coordinating residues; violet, Cl^- coordinating residues; gray, Na^+ coordinating residues in NKCC1; yellow, disulfide bond forming residues; brown, glycosylated residues; cyan, extracellular gate forming residues; black, putative dimerization interfaces. (B) Cladogram of CCC family made using sequences from mouse. (C) Percentage sequence identity between members of the mouse CCC family.

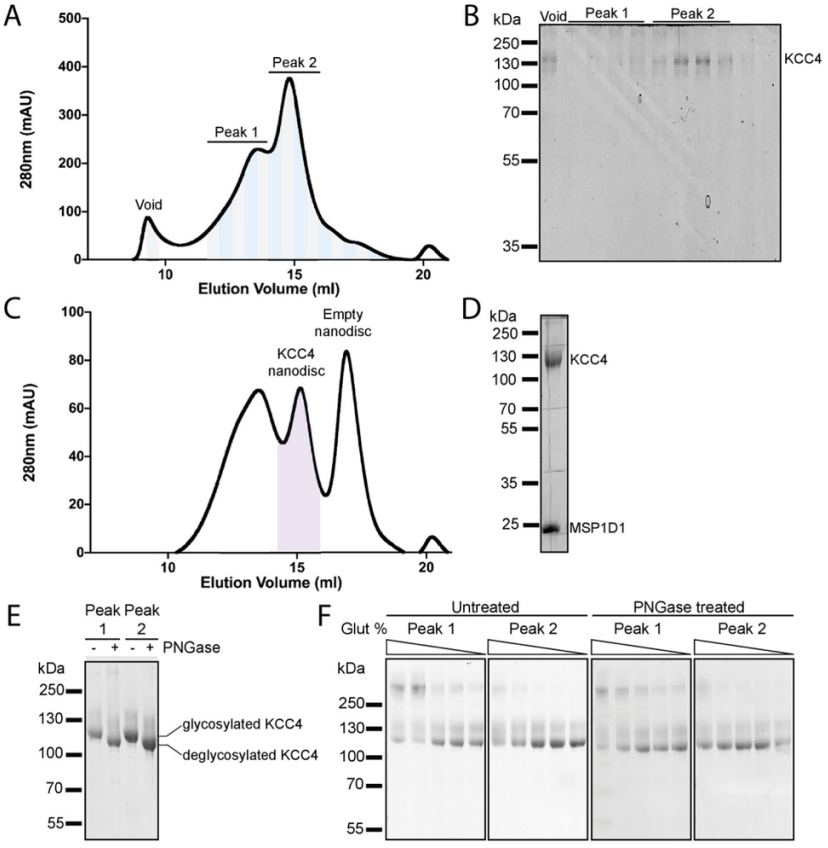

Figure 2 supplement 2: Purification and reconstitution of mouse KCC4. (A) Representative chromatogram from a Superose six gel filtration of KCC4 purified in DDM/CHS. (B) Coomassie-stained SDS-PAGE fractions (indicated by alternating gray and blue bands in (A)) with band corresponding to KCC4 labeled. KCC4 is present in two species: an earlier eluting, broader peak one and a later eluting, sharper peak 2. Fractions in the later eluting peak correspond to monodisperse KCC4 and were used for structure determination. (C) Representative chromatogram from Superose six gel filtration of KCC4 reconstituted in MSP1D1 lipid nanodiscs. (D) Coomassie-stained SDS-PAGE of final pooled KCC4-MSP1D1 nanodisc sample (indicated by purple shading in (C)). (E) Coomassie-stained SDS-PAGE of peak 1 and peak two pools (as indicated in (A,B)) before (-) and after (+) treatment with PNGase. (F) Coomassie-stained SDS-PAGE of KCC4 crosslinked with different concentrations of glutaraldehyde (bands within each gel correspond to 0.02, 0.01, 0.005, 0.0025, and 0% glutaraldehyde, respectively). Peak 1 and peak two samples were pooled as indicated in (A,B), concentrated, and crosslinked (left pair of gels) or deglycosylated with PNGase prior to crosslinking (right pair of gels).

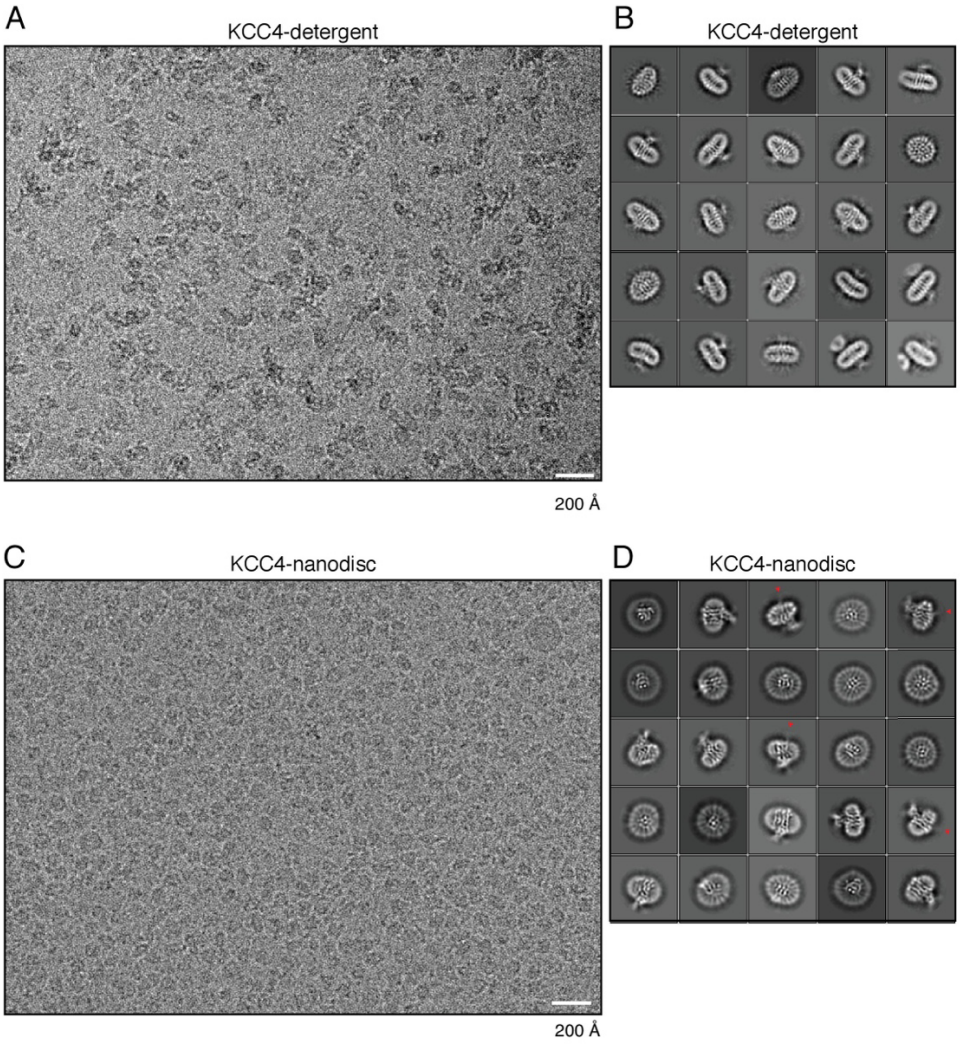

Figure 2 supplement 3: Example micrograph and 2D class averages. (A) Representative micrograph and (B) selected class averages of KCC4 in detergent (DDM/CHS) micelles. (C) Representative micrograph and (D) selected class averages of KCC4 in MSP1D1 lipid nanodiscs. Red arrowheads in (D) point to blurred density features on the intracellular side of the membrane consistent with flexible N-terminal regions or CTDs.

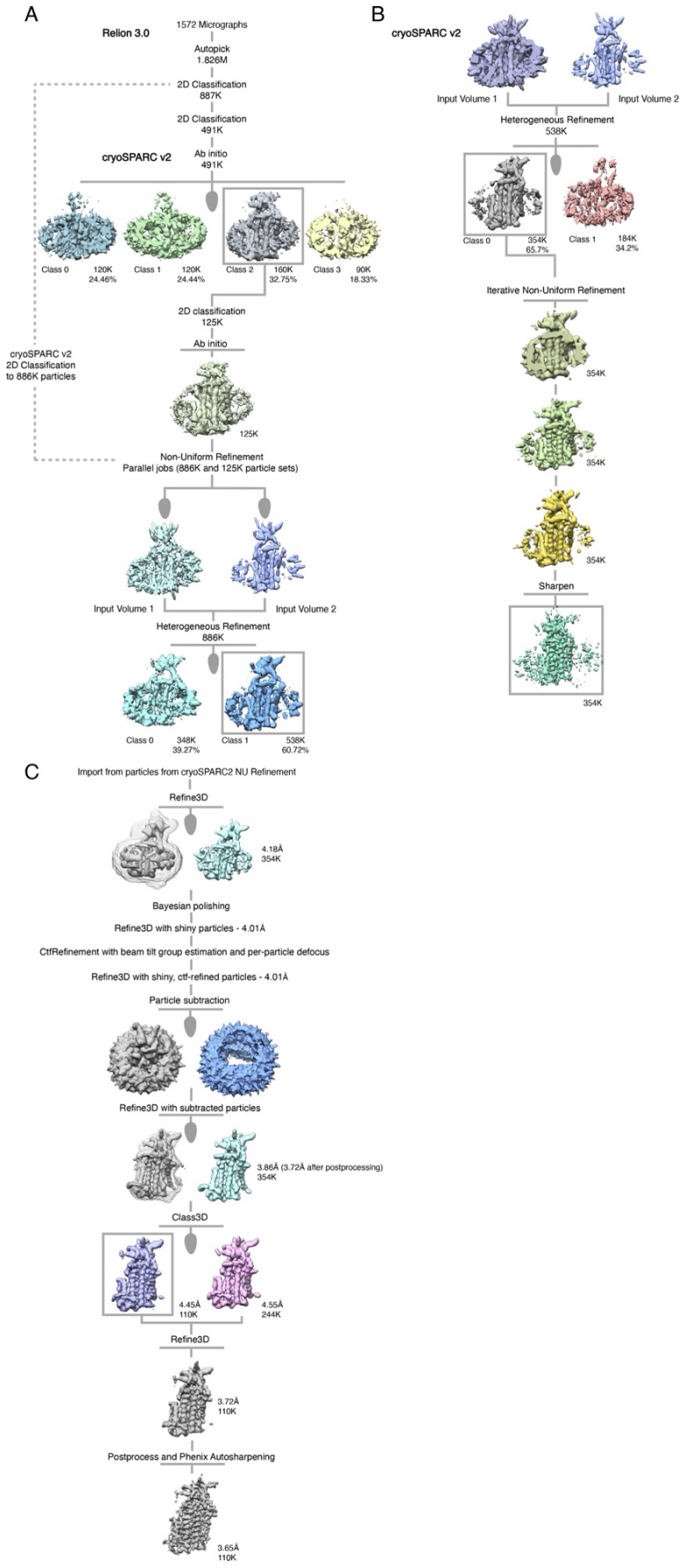
A
Relion 3.0
1572 Micrographs
Autopick
1.826M
2D Classification
887K
2D Classification
491K
cryoSPARC v2
Ab initio
491K
Class 0
120K
24.46%
Class 1
120K
24.44%
Class 2
160K
32.75%
Class 3
90K
18.33%
2D classification
125K
Ab initio
125K
cryoSPARC v2
2D Classification
to 886K particles
Non-Uniform Refinement
Parallel jobs (886K and 125K particle sets)
Input Volume 1
Input Volume 2
Heterogeneous Refinement
886K
Class 0
348K
39.27%
Class 1
538K
60.72%
B
cryoSPARC v2
Input Volume 1
Input Volume 2
Heterogeneous Refinement
538K
Class 0
354K
65.7%
Class 1
184K
34.2%
Iterative Non-Uniform Refinement
354K
354K
354K
Sharpen
354K
C
Import from particles from cryoSPARC2 NU Refinement
Refine3D
4.18Å
354K
Bayesian polishing
Refine3D with shiny particles - 4.01Å
CtfRefinement with beam tilt group estimation and per-particle defocus
Refine3D with shiny, ctf-refined particles - 4.01Å
Particle subtraction
Refine3D with subtracted particles
3.86Å (3.72Å after postprocessing)
354K
Class3D
4.45Å
110K
4.55Å
244K
Refine3D
3.72Å
110K
Postprocess and Phenix Autosharpening
3.65Å
110K

Figure 2 supplement 4: Cryo-EM processing pipeline for KCC4 in MSP1D1 nanodiscs. (**A, B**) Initial stages of cryo-EM data processing in Relion and cryoSPARC2. (**C**) Final stages of cryo-EM data processing in Relion. See Materials and methods for details.

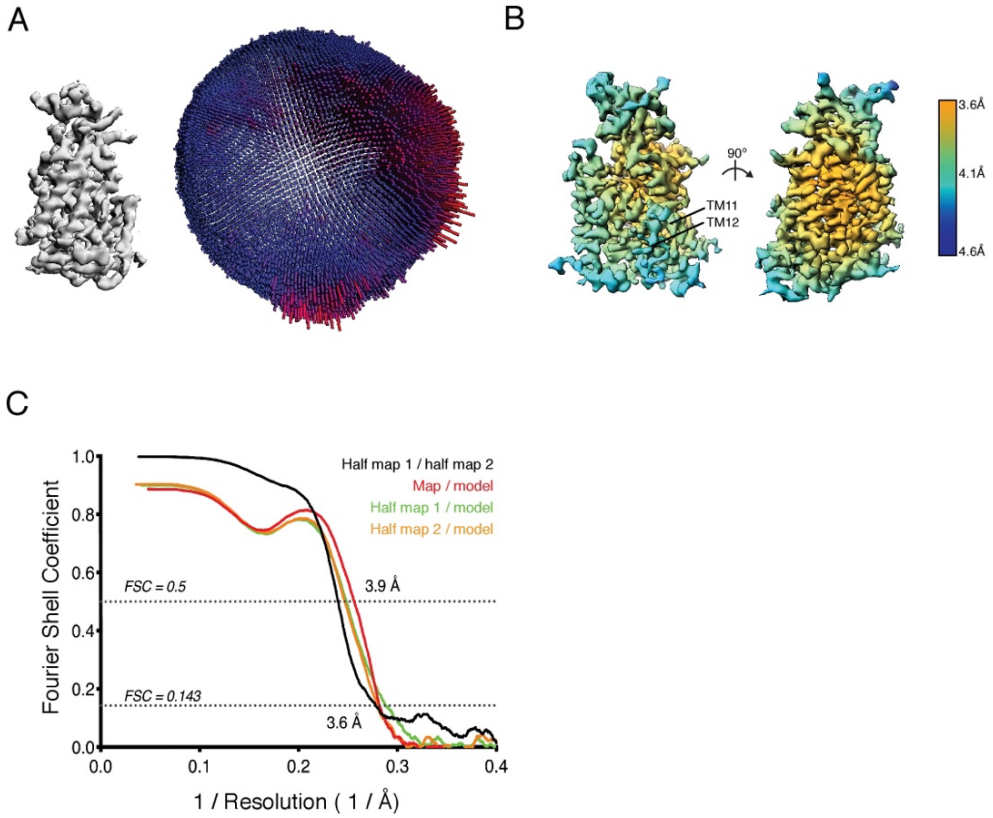

Figure 2 supplement 5: Cryo-EM validation. (**A**) Angular distribution of particles used in final refinement with final map for reference. (**B**) Local resolution estimated in Relion colored as indicated on the final map. (Right) A view from the membrane plane showing relatively weaker local resolution in TM11-12 and (left) a view rotated 90°. (**C**) Fourier Shell Correlation (FSC) relationships between (black) the two unfiltered half-maps from refinement and used for calculating overall resolution at 0.143, (red) final map versus model, (orange) half-map one versus model, and (green) half-map two versus model.

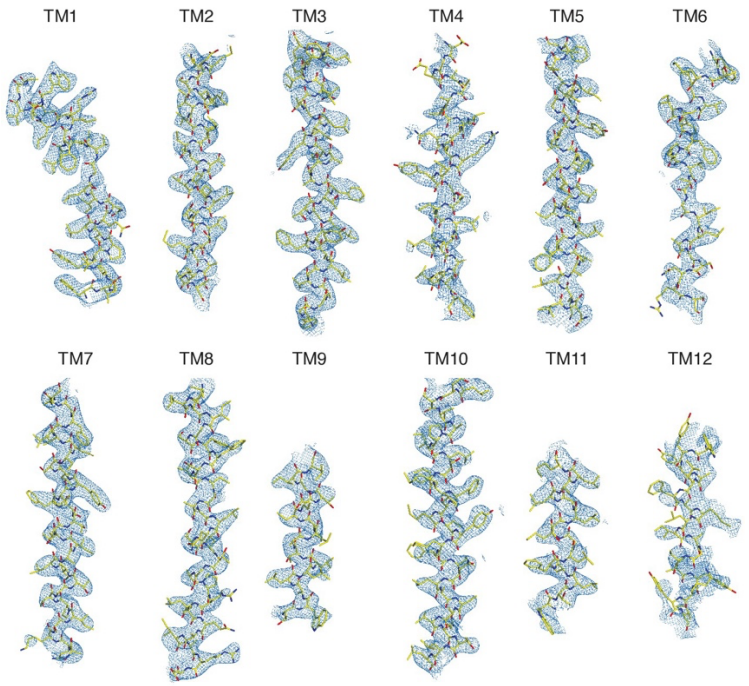

Figure 2 supplement 6: Representative regions of cryo-EM map. Cryo-EM density is shown carved around each transmembrane helix with the atomic model of KCC4 drawn as sticks.

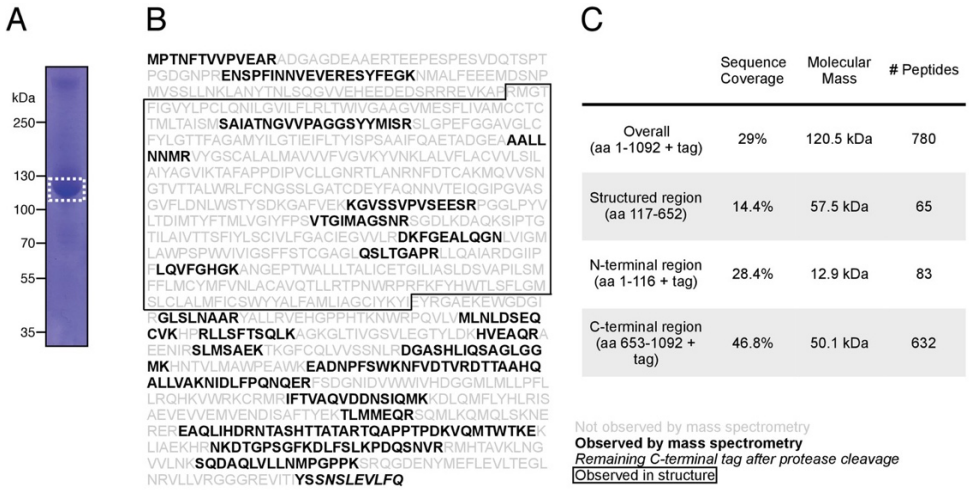

	Sequence Coverage	Molecular Mass	# Peptides
Overall (aa 1-1092 + tag)	29%	120.5 kDa	780
Structured region (aa 117-652)	14.4%	57.5 kDa	65
N-terminal region (aa 1-116 + tag)	28.4%	12.9 kDa	83
C-terminal region (aa 653-1092 + tag)	46.8%	50.1 kDa	632

Figure 2 supplement 7: Mass spectrometry of purified KCC4. (**A**) Coomassie-stained SDS-PAGE of purified mouse KCC4 sample used for mass spectrometry. The band indicated by dashed line box was excised for analysis. (**B**) Identified peptides (bold) are indicated on the purified KCC4 sequence. Boxed region indicates boundaries of KCC4 observed by cryo-EM. (**C**) Summary of mass spectrometry data.

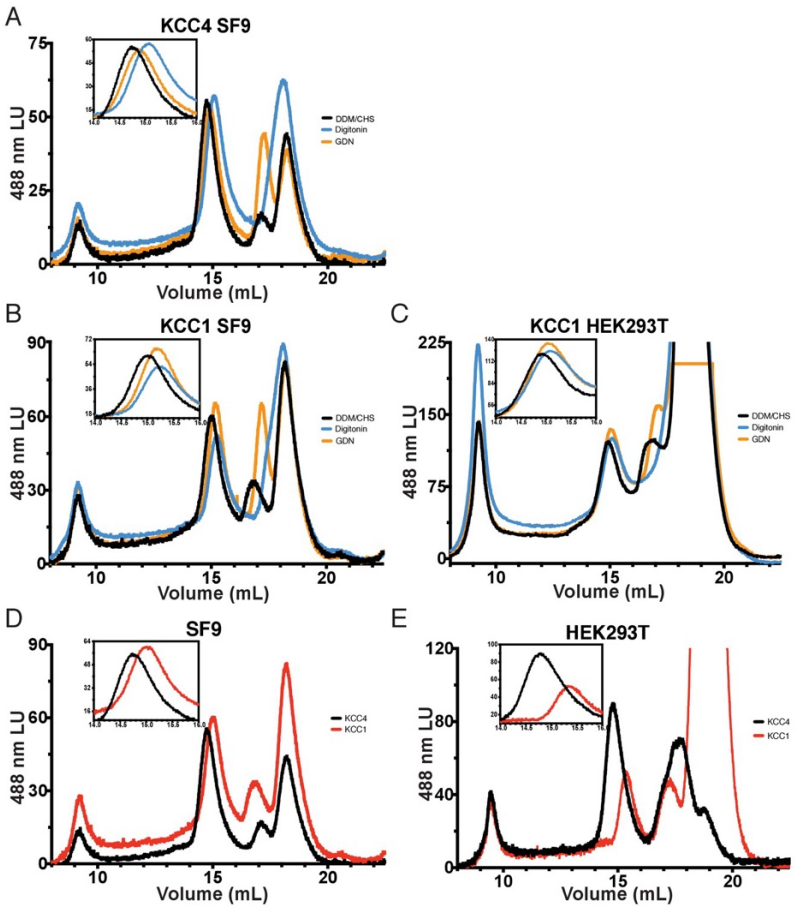

Figure 2 supplement 8: FSEC comparison of KCC4 and KCC1 expressed in different host cells and treated with different detergents. (**A**) Overlaid fluorescence chromatograms from a Superose six gel filtration of KCC4 expressed in SF9 cells and extracted/run in DDM:CHS/DDM:CHS (black; conditions used in KCC4 structure determination) DDM:CHS/GDN (orange; conditions used in KCC1 structure determination), and LMNG/digitonin (blue; conditions used in NKCC1 structure determination). (**B**) As in (**A**), but for KCC1 expressed in SF9 cells. (**C**) As in (**A**), but for KCC1 expressed in HEK293T cells. (**D**) Overlaid fluorescence chromatograms of KCC4 (black) and KCC1 (red) expressed in SF9 cells and extracted/run in DDM:CHS/DDM:CHS. (**E**) As in (**D**), but for KCC4 (black) and KCC1 (red) expressed in KEK293T cells.

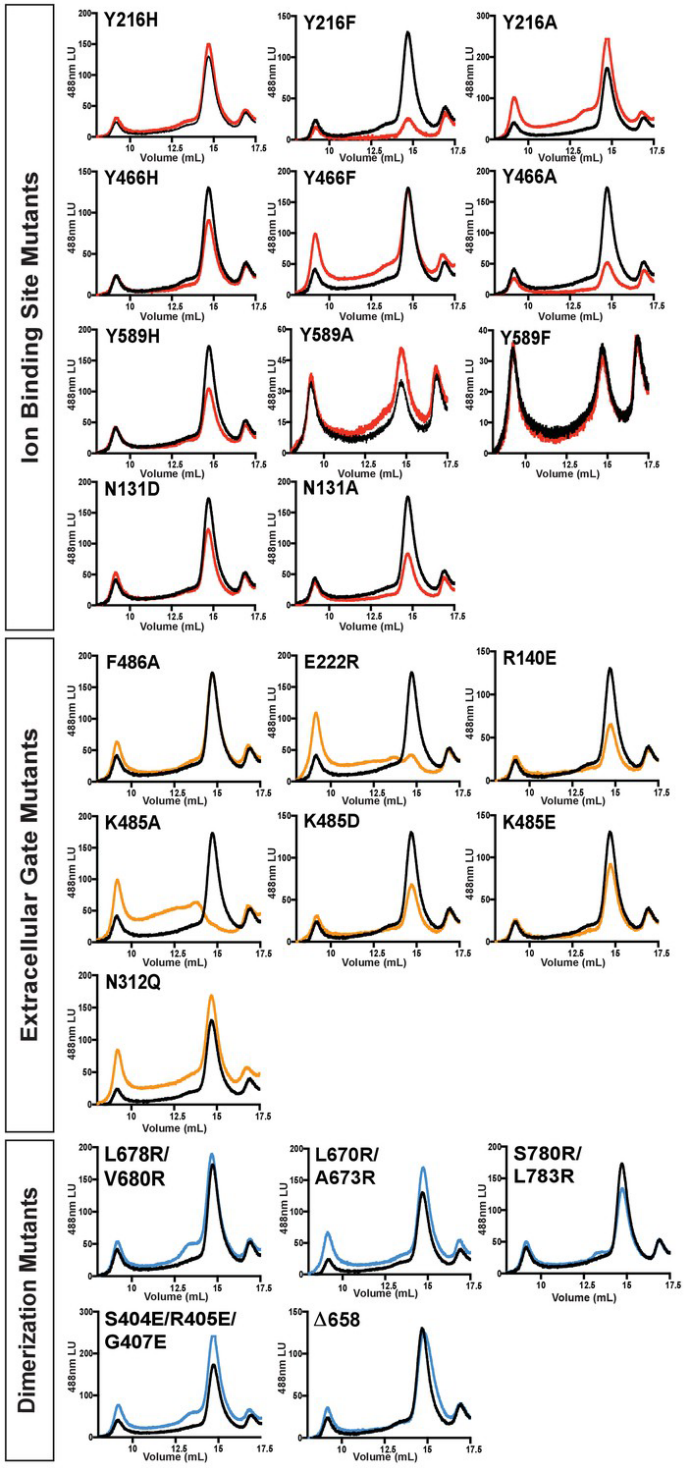

Figure 3 supplement 1: FSEC comparison of KCC4 mutations. Representative fluorescence chromatograms from a Superose six gel filtration of wild-type KCC4-GFP (black) compared to each mutant KCC4-GFP. Traces for mutations in ion binding sites are colored red, mutations in the extracellular gate are colored orange, and mutations in putative dimerization interfaces are colored blue.

Table 1. Cryo-EM data collection and structure refinement statistics	
Data collection	
Total movie #	1572
Selected movie #	1401
Magnification	36,000x
Voltage (kV)	200
Electron exposure (e–/A° 2)	46.665
Frame #	50
Defocus range (um)	-0.7 to -2.5
Super resolution pixel size (A°)	0.5685
Binned pixel size (A°)	1.137
Processing	
Initial particle images (no.)	887,132
Final particle images (no.)	110,143
Map resolution	
Masked (A° , FSC = 0.143/ FSC=0.5)	3.6/4.2
Unmasked (A° , FSC = 0.143/ FSC=0.5)	3.9/4.4
Refinement	
Model resolution (A° , FSC = 0.143/ FSC=0.5)	3.5/3.9
Map-sharpening B factor (A° 2)	-150
Composition	
Number of atoms	4103
Number of protein residues	536
Ligands total	4
K+	1
Cl-	1
NAG-NAG-BMA	2
R.m.s. deviations	
Bond lengths (A°)	0.005
Bond angles (°)	0.731
Validation	
MolProbity score	1.7
Clashscore	4.59
EMRinger score	1.74
Ramachandran plot	
Favored (%)	92.48
Allowed (%)	7.52
Disallowed (%)	0
Rotamer outliers (%)	0.23
Mean *B* factors (A° ^{2})	
Protein	75.41
Ligand	106.62

Table 2: Key resources table				
Reagent type (species) or resource	Designation	Source or reference	Identifiers	Additional information
Gene (Mus musculus)	KCC4	Synthesized (Thermo Fisher)	Uniprot Q80WG5	Codon-optimized for Spodoptera frugiperda
Gene (Mus musculus)	KCC1	Synthesized (Thermo Fisher)	Uniprot Q9QY75	Codon-optimized for Spodoptera frugiperda
Recombinant DNA reagent	pACEBAC1	Geneva Biotech	pACEBac1	Modified as described in Materials and methods
Cell Line (Spodoptera frugiperda)	Sf9	Expression Systems	Catalog Number: 94–001F	
Cell Line (H. sapiens)	HEK293T	ATCC	Catalog Number: CRL-3216	
Cell Line (H. sapiens)	HEK293T GnTI-	ATCC	Catalog Number: CRL-3022	
Peptide, recombinant protein	MSP1D1	Prepared as described in doi: 10.1016/S0076-6879(09)64011–8		His-tag cleaved
Chemical compound	DDM	Anatrace	Part Number: D310S	
Chemical compound	CHS	Anatrace	Part Number: CH210	
Chemical compound	Digitonin	EMD Chemicals	CAS 11024-24-1	
Chemical compound	GDN	Anatrace	Part Number: GDN101	
Chemical compound	18:1 (D9-Cis) PE (DOPE) lipid	Avanti Polar Lipids	SKU: 850725C	
Chemical compound	16:0-18:1 PS (POPS) lipid	Avanti Polar Lipids	SKU: 840034C	
Chemical compound	16:0-18:1 PC (POPC) lipid	Avanti Polar Lipids	SKU: 850457C	
Chemical compound	FluxOR Red Potassium Ion Channel Assay	ThermoFisher Scientific	Catalog Number: F20019	
Software, algorithm	RELION	DOI: 10.7554/eLife.42166	Relion 3.0.7	

Software, algorithm	Cryosparc	DOI: 10.1038/nmeth.4169	Cryosparc2	
Software, algorithm	Ctffind	doi: 10.1016/j.jsb.2015.08.008	Ctffind 4.1.13	
Software, algorithm	PyEM	doi: 10.5281/zenodo.3576630.	PyEM https://zenodo.org/record/3576630#.XmptWJNKjUI	
Software, algorithm	UCSF Chimera	UCSF	RRID:SCR_004097	http://plato.cgl.ucsf.edu/chimera/
Software, algorithm	COOT		RRID:SCR_014222	http://www2.mrc-lmb.cam.ac.uk/personal/pemsley/coot/
Software, algorithm	Phenix		RRID:SCR_014224	https://www.phenix-online.org/
Software, algorithm	PyMOL	PyMOL Molecular Graphics System, Schrodinger LLC	RRID:SCR_000305	https://www.pymol.org/

Chapter 3: Concluding remarks

3.1 Structural insights from recent cryo-EM CCC structures

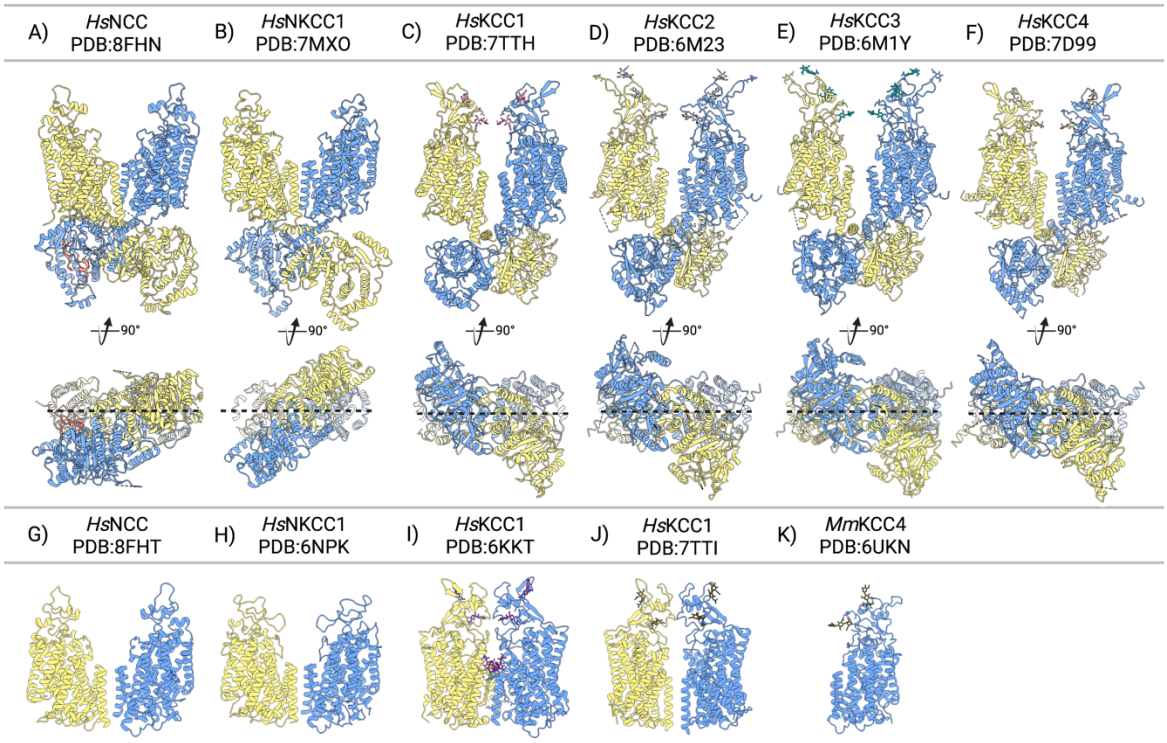

Figure 1. A collection of representative CCC structures.
All CCCs are shown in their dimeric form (A-J), except for MmKCC4 (K), which can also exist as a monomer. The intracellular view of each dimer is also presented by rotating each 90° degrees. Subunits in each dimer are colored yellow or blue. The NKCC1 N-terminal domain is depicted in salmon (A). Deposited structures with unresolved C-terminal domains are shown in (G-K).

Since 2019, significant progress has been made in visualizing the structures of the CCC family, which includes NKCC1 [15, 1, 18], NCC [6], and KCC1-4 [10, 2, 14, 3, 9, 19] . The solved CCCs structures confirmed the predicted LeuT-fold and revealed the architecture of the extracellular (ECD) and C-terminal domain (CTD). The TMD is composed of two pseudosymmetric five-helix bundles of inverted repeats, with dimerization between TMD subunits mediated by TM11 and TM12. Interestingly, the TMD of all CCCs, whether in outward-open or inward-open states, have been found to superimpose well, while the cytoplasmic and extracellular domains varied in overall structure, tilt, and/or rotation. The ECD, located between TM7 and TM8 in Na^+-dependent CCCs and between TM5 and TM6 in Na^+-independent CCCs, formed highly diverse structures, with some playing a role in dimerization. In the *Hs*KCC2-4 structures, the N-terminal domain occupied the cytosolic-facing cavity, mediating autoinhibition, while in NKCC1, the NTD interacted tightly with the surface of the C-terminal domain of the second protomer [2].

The CCCs have demonstrated a dimeric assembly in addition to *Mm*KCC4 [9] which was also been determined in monomeric form. In dimeric CCC structures, one protomer's CTD is positioned directly beneath the TMD of the other protomer connected by a scissor helix extending from

TM12 forming a closely bound CTD dimer. This CTD dimer is held together by the largest dimeric interface in the CCCs structure which implies its influence on the overall dimeric arrangement. In structures where the CTD is unresolved (CTD possibly monomeric), multiple TMD dimer arrangements are observed. For example, in *Hs*KCC2 structures where the ECD, TMD, and CTD are clearly resolved, the TMD dimerization interface involves TM11 and TM12. However, in *Hs*KCC2TMD where the CTD is not visible, the TMD dimerization interface is mediated solely by two parallel TM12 helices. Since the TMD dimer interface is comparably loose, it is possible that closely engaged CTD dimers restrict the TMD dimeric interface resulting in tighter and less variable arrangements.

The CCC structures have a small interaction surface between the CTD and TMD, which allows for flexibility between these two domains. Studies on *Dr*NKCC1 have shown that the two domains can undergo different motions, such as tilting and rotating, with transient interactions occurring at multiple contact points between them [1]. For example, in *Dr*NKCC1, one CTD subunit is slightly tilted up and closer to the intracellular vestibule, while in *Hs*KCC2-4, the CTDs are not tilted but rotated clockwise by 70° degrees [1]. These movements, along with the different dimeric arrangements and CTD dimer positions, could play a role in allowing or inhibiting access to the intracellular vestibule. Post-translational modifications on the CTD or NTD can also affect TMD-CTD interactions by inhibiting autoinhibition like in KCCs or promoting transport activity via an unknown mechanism in N(K)CCs.

3.2 The inhibitor-bound outward-open state in CCCs

All CCC structures have been resolved in the inward-open conformation, which is the more stable conformation. The NKCC1 and KCC1 outward-open structures were facilitated by wedging inhibitors into the extracellular permeation pathway, specifically by binding inhibitors (VU0463271 for KCC1; bumetanide and furosemide for NKCC1) deep into the pathway[18]. Superimposition of drug-bound NKCC1 and KCC1 shows that bumetanide, furosemide, and VU0463271 bind to the same region within the extracellular vestibule, and each function as a molecular wedge to stabilize the outward-open structure.

The high-resolution structure of NKCC1 with bound bumetanide has been solved at 2.9Å, providing insight into how structurally similar loop diuretics bind. Bumetanide has a cross-shaped structure, with a central benzene ring and four orthogonal arms that fit into the extracellular vestibule formed by TM1b, TM6b, TM3, and TM10. It coordinates with K^+ and co-occludes the Cl^- ion at site 2, with the carboxy group occupying Cl^- at site 1 [18]. The sulfamyl group at the outermost end of the extracellular vestibule interacts with Ile493 of TM6a which explains why non-sulfonamide loop diuretics are less potent. The phenoxyl group opposite the sulfamyl group at the outer edge of the extracellular vestibule forms several interactions with residues on TM3 and TM10. Furosemide lacks this phenoxyl group and has a chlorine atom,

which makes it approximately 50-fold less potent than bumetanide. Lastly, the butylamino group located deeper into the extracellular ion pathway forms hydrophobic interactions with Met382 and Tyr383 on TM3, and Pro496 and Thr499 on TM6a. Substitutions of Met382 abolish bumetanide inhibition.

In a similar manner, VU0463271 in the KCC1 structure fits into the extracellular pocket formed by TM1b, TM6a, TM3, and TM10, where it forms multiple polar and hydrophobic contacts along the extracellular ion pathway [19]. At the outermost edge, the 4-methyl-2-thiazolyl group forms contacts with Arg140 and Glu222, which disrupt the salt bridge critical in extracellular gate closure. The 4-methyl-2-thiazolyl group forms several hydrogen bonding and hydrophobic interactions along TM3 and TM1b. Deeper into the extracellular vestibule, the phenyl-3-pyridazinyl group coordinates with several residues on TM6a, TM3, and TM10, some of which participate in coordinating the permeating K^+ ion. Met215, an equivalent residue to M382 in NKCC1, also results in a ~65-fold loss in sensitivity to VU0463271 inhibition upon substitution to alanine. These sites may be essential ligand-binding sites in the CCC family. Taken together, these drug-bound structures highlight a hotspot for pharmacological inhibition and set a foundation for improving the specificity and potency of these widely prescribed drugs.

3.3 Alternating access mechanism in CCCs

In NKCC1 and KCC1, the extracellular pathway is opened by disrupting the salt bridge between TM1b and TM3 and moving TM3, TM9, and TM10 away from the extracellular permeation pathway. On the cytosolic end, the intracellular vestibule closes when TM8 and TM4 move towards the center of the ion pathway. VU0463271 directly engages TM3 and TM10, pushing them away from the center of the extracellular vestibule. Mutagenesis experiments on TM3 and TM10 have shown effects on translocation rate, ion affinities, and loop diuretic affinities, supporting their prominent role in ion translocation [4].

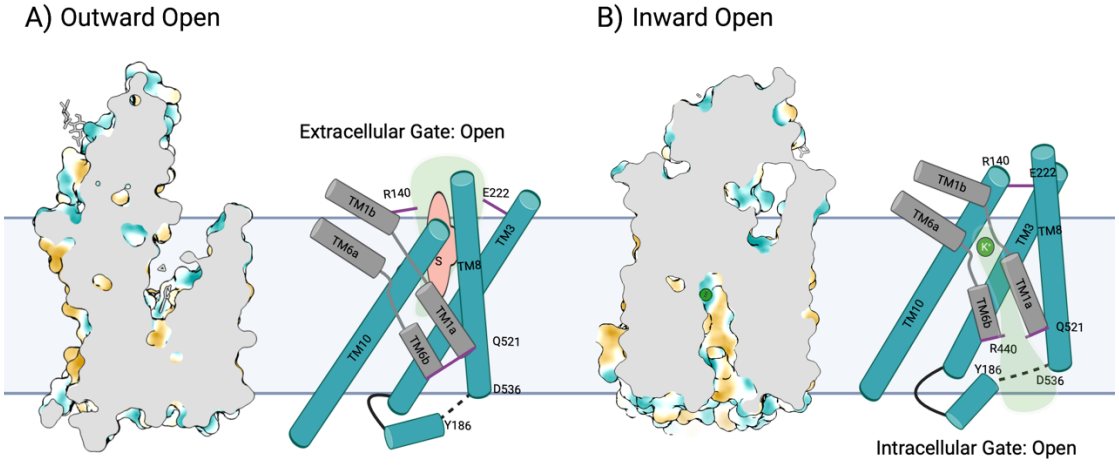

Created with BioRender.com

Figure 2. Model of CCC gating interactions and conformational changes.
In the inward-open (B) state the intracellular gate is open and while the salt bridge R140-E222 is closed. The

outward-open state (A) was captured by wedging VU0463271 into the extracellular ion permeation pathway (Zhao, 2021). The substrate directly engages transmembrane helices TM3 and TM10, breaking the extracellular gate, disrupting K+ coordination, and triggering the concerted movement of TM3, TM8, and the intracellular loop 1 (ICL1) helix, as well as the subtle movement of TM10. These movements foster gating interactions (R440-Q521) that close the intracellular vestibule.

In LeuT and other APC transporters, the two discontinuous transmembrane domains, TM1 and TM6, act as a hinge by opening and closing the intra- and extracellular gates to access the binding pocket. Surprisingly, the outward-open structure of CCCs showed overall subtle structural rearrangements that differ from the canonical alternating access mechanisms observed in LeuT-fold transporters. In NKCC1 and KCC1, the bundle helices (TM1, TM6, TM2, and TM7) remain static, and the scaffolding helices (TM3, TM8, TM4, and TM9) undergo displacement. According to the alternating access model, the opening of the extracellular gate requires the closure of the intracellular gate. However, CCCs accomplish this without hinge movements by TM1 and TM6. Previous observations on the catalytic rate of CCCs described it as orders of magnitude faster than related transporters, suggesting that the CCCs transport cycle may differ from other APC transporters [11].

3.4 N-terminal domain role in transport function

The role of the N-terminal domain (NTD) was demonstrated in work on HsKCC2 which identified an analogous mechanism to the VU0463271 inhibitor that wedges into the extracellular permeation pathway to stabilize the outward-open conformation. In contrast, the NTD stabilizes the inward-open conformation by acting as a wedge lodged into the intracellular permeation pathway. This interaction is stabilized by forming contacts with transmembrane domains (TMs) at the cytosolic vestibule. The NTD comprises three regions: N1, N2, and linker 12 (L12), and they directly interact with TM8, IL23, and the TM6b-7 loop to restrict the closure of the cytosolic vestibule. While the NTD is not highly conserved, the L12 region is conserved and forms extensive networks with TM1a, TM6b, and TM8 via hydrogen bonds, suggesting a common autoinhibition mechanism in the KCC family. Notably, the N2 helix on the CTD-facing side of the NTD contains negatively charged residues (Glu102 and Glu105), which establish electrostatic interactions with the positively charged surface of the CTD. Therefore, a dimeric state with the CTD closely engaged is likely to promote the autoinhibited state in KCCs.

In NKCC1, the NTD interacts via extensive hydrophilic interactions with the CTD of the other protomer in the domain-swapped configuration [19]. Specifically, residues Asn216 to Leu250 form extensive interactions along the face of the CTD, and any disruption in the hydrophilic interactions or buried hydrophobic residues within the NTD results in a significant loss of transport activity. For example, mutation of L243 to alanine abolished activity. One of the major phosphoacceptor sites on the NTD is Thr217, which is phosphorylated in response to cell shrinkage and forms hydrogen bonds with the CTD residue Arg1174. Weakening the interaction

by site-directed mutagenesis in Thr217 abolished NKCC1 transport activity. However, it is still unclear how charged phosphate groups at these known phosphoacceptor sites modulate NTD and CTD interactions and couple to the TMD to affect transport activity.

Major advances in our understanding of CCC transporter structure and mechanism have been realized over the past several years as a result of my thesis work and that from other groups discussed in this Chapter. Together, these studies lay the groundwork for future studies aimed at addressing outstanding questions concerning the function, modulation, and physiological roles of this important family of transporters.

3.5 References

1. Chew TA, Orlando BJ, Zhang J, Latorraca NR, Wang A, Hollingsworth SA, Chen DH, Dror RO, Liao M, Feng L. Structure and mechanism of the cation-chloride cotransporter NKCC1. Nature. 2019 Aug;572(7770):488-492. doi: 10.1038/s41586-019-1438-2. Epub 2019 Jul 31. PMID: 31367042; PMCID: PMC6856059.
2. Chi, X., Li, X., Chen, Y. et al. Cryo-EM structures of the full-length human KCC2 and KCC3 cation-chloride cotransporters. Cell Res 31, 482–484 (2021). https://doi.org/10.1038/s41422-020-00437-x
3. Chi, G., Ebenhoch, R., et al. Phospho-regulation, nucleotide binding and ion access control in potassium-chloride cotransporters. The EMBO Journal (2021) 40: e107294. https://doi.org/10.15252/embj.2020107294
4. Fang, Y., Jayaram, H., Shane, T., Kolmakova-Partensky, L., Wu, F., Williams, C., et al. (2009). Structure of a prokaryotic virtual proton pump at 3.2 . resolution. Nature 460, 1040–1043. doi: 10.1038/nature08201
5. Hediger MA, Clémençon B, Burrier RE, Bruford EA. The ABCs of membrane transporters in health and disease (SLC series): introduction. Mol Aspects Med. 2013 Apr-Jun;34(2-3):95-107. doi: 10.1016/j.mam.2012.12.009. PMID: 23506860; PMCID: PMC3853582.
6. Jing Nan et al. Cryo-EM structure of the human sodium-chloride cotransporter NCC.*Sci. Adv.*8,eadd7176(2022).DOI:10.1126/sciadv.add7176
7. Krishnamurthy H, Gouaux E. X-ray structures of LeuT in substrate-free outward-open and apo inward-open states. Nature. 2012 Jan 9;481(7382):469-74. doi: 10.1038/nature10737. PMID: 22230955; PMCID: PMC3306218.
8. Portioli, C., Munevar, MJR., et al. Cation-coupled chloride cotransporters: chemical insights and disease implications. Trends in Chemistry, (2021), Vol. 3, No. 10. https://doi.org/10.1016/j.trechm.2021.05.004
9. Reid MS, Kern DM, Brohawn SG. Cryo-EM structure of the potassium-chloride cotransporter KCC4 in lipid nanodiscs. Elife. 2020 Apr 14;9:e52505. doi: 10.7554/eLife.52505. PMID: 32286222; PMCID: PMC7200160.

10. Si Liu et al. Cryo-EM structures of the human cation-chloride cotransporter KCC1.*Science*366,505-508(2019).DOI:10.1126/science.aay3129
11. Somasekharan, S., Tanis, J. E., Kim, J. Y., Oh, B. C., and Gagnon, K. B. (2012). Loop diuretic and ion-binding residues revealed by scanning mutagenesis of transmembrane helix 3 (TM3) of Na-K-Cl cotransporter (NKCC1). Journal of Biological Chemistry, 287(22), 18190–18199. doi: 10.1074/jbc.M111.323105
12. Weber, M., Hartmann, A.-M., Beyer, T., Ripperger, A., and Nothwang, H. G. "A novel regulatory locus of phosphorylation in the C-terminus of the potassium chloride cotransporter KCC2 that interferes with N-ethylmaleimide or staurosporine mediated activation." Journal of Biological Chemistry, vol. 289, 2014, pp. 18668–18679. doi:10.1074/jbc.M114.567834.
13. Weng, TY, Chiu, WT, Liu, HS, Cheng, HC, Shen, MR, Mount, DB, and Chou, CY. "Glycosylation regulates the function and membrane localization of KCC4." Biochimica et Biophysica Acta, vol. 1833, no. 5, 2013, pp. 1133-1146. Doi:10.1016/j.bbamcr.2013.01.018. PMID: 23376777.
14. Xie Y, Chang S, Zhao C, Wang F, Liu S, Wang J, Delpire E, Ye S, Guo J. Structures and an activation mechanism of human potassium-chloride cotransporters. Sci Adv. 2020 Dec 11;6(50):eabc5883. doi: 10.1126/sciadv.abc5883. PMID: 33310850; PMCID: PMC7732191.
15. Yang, X., Wang, Q. & Cao, E. Structure of the human cation–chloride cotransporter NKCC1 determined by single-particle electron cryo-microscopy. Nat Commun 11, 1016 (2020). https://doi.org/10.1038/s41467-020-14790-3
16. Zhang, S., Zhou, J., Zhang, Y. et al. The structural basis of function and regulation of neuronal cotransporters NKCC1 and KCC2. Commun Biol 4, 226 (2021). https://doi.org/10.1038/s42003-021-01750-w
17. Zhao Y, Cao E. Structural Pharmacology of Cation-Chloride Cotransporters. Membranes (Basel). 2022 Nov 29;12(12):1206. doi: 10.3390/membranes12121206. PMID: 36557113; PMCID: PMC9784483.
18. Zhao, Y., Roy, K., Vidossich, P. *et al.* Structural basis for inhibition of the Cation-chloride cotransporter NKCC1 by the diuretic drug bumetanide. *Nat Commun* 13, 2747 (2022). https://doi.org/10.1038/s41467-022-30407-3
19. Zhao, Yongxiang, et al. "Structure of the Human Cation–Chloride Cotransport KCC1 in an Outward-Open State." Proceedings of the National Academy of Sciences of the United States of America, vol. 119, no. 27, (2022), e2109083119. doi: 10.1073/pnas.2109083119.